HHS Public Access

Author manuscript

Nat Immunol. Author manuscript; available in PMC 2023 January 01.

Published in final edited form as:

Nat Immunol. 2022 July ; 23(7): 1063–1075. doi:10.1038/s41590-022-01231-0.

pH sensing controls tissue inflammation by modulating cellular metabolism and endo-lysosomal function of immune cells

Xiangjun Chen[1,2,3,4], **Alok Jaiswal**[1], **Zachary Costliow**[1], **Paula Herbst**[2,3], **Elizabeth A. Creasey**[1,2,3], **Noriko Oshiro-Rapley**[1,2,3,4], **Mark J. Daly**[1,5,6], **Kimberly L. Carey**[1], **Daniel B. Graham**[1,2,3,4,7], **Ramnik J. Xavier**[1,2,3,7,*]

[1]Broad Institute of MIT and Harvard, Cambridge, MA 02142, USA

[2]Center for Computational and Integrative Biology, Massachusetts General Hospital, Boston, MA 02114, USA

[3]Department of Molecular Biology, Massachusetts General Hospital, Boston, MA 02114, USA

[4]Experimental Medicine Unit, Massachusetts General Hospital, Harvard Medical School, Boston, MA 02114, USA

[5]Analytic and Translational Genetics Unit, Massachusetts General Hospital, Harvard Medical School, Boston, MA 02114, USA

[6]Institute for Molecular Medicine Finland (FIMM), Helsinki, Finland

[7]Klarman Cell Observatory, Broad Institute of MIT and Harvard, Cambridge, MA 02142, USA

Abstract

Extracellular acidification occurs in inflamed tissue and the tumor microenvironment; however, a systematic study on how pH sensing contributes to tissue homeostasis is lacking. Here, we examine cell type-specific roles of the pH sensor GPR65 and its inflammatory disease-associated I231L coding variant in inflammation control. GPR65 I231L knock-in mice are highly susceptible to both bacterial infection-induced and T cell-driven colitis. Mechanistically, GPR65 I231L elicits a cytokine imbalance through impaired Th17 and Th22 differentiation and IL-22 production in association with altered cellular metabolism controlled through the cAMP-CREB-DGAT1 axis. In dendritic cells, GPR65 I231L elevates IL-12 and IL-23 release at acidic pH and alters endo-lysosomal fusion and degradation capacity, resulting in enhanced antigen presentation. This study highlights GPR65 I231L as a multistep risk factor in intestinal inflammation and illuminates a mechanism by which pH sensing controls inflammatory circuits and tissue homeostasis.

*Correspondence: xavier@molbio.mgh.harvard.edu.

AUTHOR CONTRIBUTIONS

R.J.X. and X.C. conceived of the study. X.C. designed and conducted most of the experiments. A.J. analyzed the scRNA-seq data. Z.C. performed the lipidomic and metabolomic experiments. P.H. and E.A.C. helped with the mouse experiments. N.O.-R. helped with immunoblotting. M.J.D. helped with genetics. X.C. wrote the manuscript. A.J., M.J.D., K.L.C., D.B.G. and R.J.X. revised the manuscript. K.L.C., D.B.G. and R.J.X. supervised the research.

COMPETING INTERESTS

R.J.X. is co-founder of Jnana Therapeutics and Celsius Therapeutics, and M.J.D. is a scientific founder of Maze Therapeutics; these organizations had no roles in this study. The remaining authors declare no competing interests.

CODE AVAILABILITY

Code used for this study is available at https://gitlab.com/xavier-lab-computation/public/gpr65-scrnaseq.

INTRODUCTION

Receptors on different cell types within tissue sense the microenvironment and are crucial for the maintenance of homeostasis. In particular, the sensing of local extracellular pH is important to regulate physiological responses to stress or sensory stimuli[1, 2, 3]. Tissue acidification occurs during inflammation and tumorigenesis, and evidence suggests that aberrant sensing and responses to environmental cues play key roles in the initiation and progression of inflammatory diseases[4, 5, 6].

The family of pH-sensitive G protein-coupled receptors (GPCRs) includes GPR4, GPR65 and GPR68[3]. GPR65 is highly expressed in various immune cell populations and is associated with chronic inflammatory diseases such as inflammatory bowel disease (IBD), multiple sclerosis and asthma[7, 8, 9, 10, 11]. Loss of GPR65 triggers inflammatory macrophage and neutrophil infiltration in a murine DSS model[12] and impairs bacterial restriction in a *Citrobacter rodentium* infection model[10], thus increasing colitis susceptibility. Moreover, GPR65 deficiency in invariant natural killer cells exacerbates disease phenotypes in an experimental autoimmune encephalomyelitis model[8], and *Gpr65*-null mice develop more severe atopic dermatitis in the MC903 model[13]. *Gpr4* and *Gpr68* are upregulated in the colonic tissue of patients with IBD and their deficiency ameliorates colitis in the *Il10*-null murine model; these observations may involve dysregulation of barrier function, indicating important regulatory roles for GPR4 and GPR68 in mucosal inflammation[14, 15]. There are, however, no reported genetic variants of *Gpr4* and *Gpr68* correlated with inflammatory diseases.

The association of the *Gpr65* locus with IBD implicates a set of 17 variants in linkage disequilibrium, including one coding variant with a substitution of isoleucine to leucine at codon 231 (I231L)[10]. Functional characterization of GPR65 I231L expression in HeLa cells demonstrated reduced cAMP induction upon receptor activation by acidic pH[10] and impaired lysosomal activity during clearance of intracellular bacterial pathogens *in vitro*[10]. However, the impacts of GPR65 I231L in a cell type-specific manner *in vivo* during physiological homeostasis and inflammation remain to be determined and are critical for understanding how dysfunction of pH sensing by GPR65 I231L confers risk of inflammatory pathologies in humans.

Here we demonstrate that GPR65 I231L mice displayed impaired antibacterial responses in the *C. rodentium* infection model and increased inflammation in the T cell transfer model of chronic colitis, with decreased IL-17A$^+$ and IL-22$^+$ CD4$^+$ T cells and elevated inflammatory cell infiltrates and cytokine production. Single-cell transcriptome profiling, flux balance analysis and metabolomics profiling indicated that fatty acid metabolism and triacylglyceride biosynthesis were tuned through the cAMP-CREB-DGAT1 axis to disfavor IL-22 and IL-17A production in GPR65-deficient helper T (Th) cells. In dendritic cells at acidic pH, inflammatory cytokine production was reduced, and GPR65 I231L specifically promoted IL-12 and IL-23 release. GPR65 I231L additionally enhanced antigen presentation to T cells due to prolonged epitope half-life resulting from delayed endo-lysosomal fusion and reduced proteolytic capacity. Together, our study provides mechanistic insights into how

a risk variant of the pH sensor GPR65 impacts inflammatory circuits *in vivo* and highlights the role of pH sensing in cellular and molecular regulation of endo-lysosomal function and T cell metabolism to maintain tissue homeostasis.

RESULTS

GPR65 I231L predisposes mice to bacteria-induced colitis

To study the effects of the *Gpr65* polymorphism *in vivo*, we generated knock-in mice harboring the murine homologue GPR65 I231L (denoted as I231L mice) using CRISPR/Cas9-based genetic manipulation (Extended Data Fig. 1a,b). We observed no evident colitis-related phenotypes in I231L mice at steady state (Extended Data Fig. 1c–e). We then examined the susceptibility of I231L mice in an induced colitis model by infecting with *C. rodentium*. Significantly higher levels of *C. rodentium* were detected in both stool and colonic tissue of *Gpr65* knockout (KO) mice compared to wild-type (WT) control mice 12 days after infection, and there was a trend toward increased bacterial burden in I231L mice (Fig. 1a; Extended Data Fig. 2a,b). Moreover, decreased colon length and histopathology analysis indicated more severe colitis in I231L and KO mice (Fig. 1b,c; Extended Data Fig. 2c). Immunophenotyping of immune cell subsets in the inflamed colon indicated that I231L and KO mice harbored higher percentages of infiltrating neutrophils and inflammatory monocytes in the colonic lamina propria (LP) (Fig. 1d,e; Extended Data Fig. 2d), which drive inflammation. When examining cytokine-producing $CD4^+$ T cell populations, we found lower percentages of IL-$17A^+$ and IL-22^+ T cells in both mesenteric lymph nodes (mLN) and colonic LP (Fig. 1f,g; Extended Data Fig. 2e). To quantify antigen-specific T cell responses, we detected IL-17A and IL-22 production by mLN immune cells after stimulation with peptide antigen derived from *C. rodentium*. We found significantly fewer IL-17A- and IL-22-producing cells in I231L and KO mice compared to WT mice (Fig. 1h,i), which is consistent with the higher bacterial burden in I231L and KO mice given that IL-22 and IL-17A can protect mice from *Citrobacter* infection[16, 17]. Analysis of cytokines in the local colonic tissue showed higher levels of inflammatory cytokines such as TNF and IL-6 in KO mice but lower levels of IL-17A, IL-22 and IL-10 in I231L and KO mice relative to WT mice (Fig. 1j; Extended Data Fig. 2f,g). Together, these results demonstrate that a single mutation in the pH sensor GPR65 dysregulates immune machinery against bacterial infection and rebalances cytokine release leading to intestinal inflammation.

Differences in bacterial burden at the later stage of *Citrobacter* infection and the changes in IL-17A- and IL-22-producing T cells indicate that GPR65 function in T cells might be pivotal for anti-*Citrobacter* responses. To study T cell intrinsic effects, we transferred primary $CD4^+$ T cells from each of the three *Gpr65* genotypes into T cell-deficient recombinase activating gene 1 (*Rag1*) KO mice, followed by *Citrobacter* infection. We again observed impaired bacterial control at the later stage of infection and decreased IL-$17A^+$ and IL-22^+ $CD4^+$ T cell populations in I231L and *Gpr65* KO T cell-transferred mice (Extended Data Fig. 2h–m), indicating that a T cell intrinsic function of GPR65 is important for protection from *Citrobacter* infection-induced colitis.

I231L impairs Th cell differentiation and IL-22 production

The decrease of IL-22 and IL-17A production in I231L mice during *C. rodentium* infection suggests the potential role of GPR65 in $CD4^+$ T cell function. We therefore explored how the I231L variant influences $CD4^+$ T cell responses. GPR65 deficiency showed no evident effects on proliferation and apoptosis of $CD4^+$ T cells upon activation *in vitro* (Extended Data Fig. 3a,b). Then, we evaluated whether GPR65 plays a role in T helper cell differentiation. *In vitro* polarization of IL-17A-producing Th17 and IL-22-producing Th22 cells was significantly reduced in I231L and KO $CD4^+$ T cells, whereas there were no changes in Th1, Th2 and induced regulatory T cell (iTreg) differentiation (Fig. 2a,b; Extended Data Fig. 3c). Consistently, there were fewer IL-$17A^+$ and IL-22^+ $CD4^+$ T cells in the small intestinal LP of I231L and KO mice (Fig. 2c), supporting a key role for GPR65 in Th17 and Th22 differentiation. Moreover, *Gpr65* expression was increased in Th17 and Th22 cells compared to other types of Th cells polarized *in vitro*, and this upregulation was confirmed at the protein level for IL-17A- and IL-22-producing $CD4^+$ T cells from the small intestinal LP (Fig. 2d).

In light of these findings and previous work demonstrating that Th17-derived, IFNγ-producing Th1-like cells are main drivers of T cell-induced colitis[18], we compared the repolarization of Th17 and Th22 cells to IFNγ-secreting cells. In these experiments, higher percentages of IFNγ-producing Th cells were repolarized from I231L-expressing or *Gpr65*-null Th17 and Th22 cells (Fig. 2e,f), suggesting that GPR65 dysfunction can elicit a pathogenic Th cell response. Next, we investigated cytokine responses of Th cells after GPR65 activation by acidic pH. Importantly, IL-22 levels were significantly induced at low (pH 6.8) relative to neutral pH in WT Th cells. However, *Gpr65* KO Th cells failed to induce IL-22 upon pH modulation, indicating GPR65-dependence (Fig. 2g; Extended Data Fig. 3d). Additionally, IFNγ and TNF production were decreased in WT Th cells and, to a lesser extent, I231L and KO Th cells upon pH reduction, while there was no consistent change in IL-17A production (Fig. 2g). Taken together, these data illustrate that GPR65 signaling regulates cytokine responses in helper T cells, and *Gpr65* KO or I231L expression impairs Th17 and Th22 differentiation.

GPR65 deficiency shifts Th22 and Th17 cell lipid metabolism

To investigate the mechanism by which GPR65 controls Th22 and Th17 cell polarization, we measured expression levels of the genes encoding Rorγt and AhR, master transcriptional regulators of Th17 and Th22, respectively[19, 20]. Both were comparably expressed among the three genotypes (Extended Data Fig. 3e), suggesting that GPR65 does not affect Th17 and Th22 polarization through regulation of Rorγt and AhR expression.

Recent studies linked cellular metabolism, especially lipid metabolism, Rorγt activity and Th17 cell function[21, 22]. We therefore took a multiomics approach to compare cellular metabolism in KO versus WT Th22 and Th17 cells. First, we determined differences in metabolic activities from transcriptomics analysis. To overcome confounding factors associated with cellular heterogeneity in Th17 and Th22 cells, we performed single-cell RNA-sequencing (scRNA-seq) of *in vitro* polarized Th17 and Th22 cells. GPR65 deficiency did not lead to major changes in cell lineage profiles but induced a decrease in the

proportion of cluster 2 cells representing a cell state that expressed higher levels of *Il17a*, *Il17f* and *Il22* (Fig. 3a; Extended Data Fig. 4a,b). Functional enrichment analysis of differentially expressed genes in cluster 2 indicated GPR65 deficiency negatively regulates T cell activation and differentiation (Fig. 3b), which is consistent with impaired Th17 and Th22 differentiation of *Gpr65*-null $CD4^+$ T cells. In Th17 cells, GPR65 deficiency was associated with increased expression of genes related to oxidative phosphorylation and ATP metabolic processes (Fig. 3b). Conversely, GPR65 deficiency showed a reduction in expression of genes regulating polyamine metabolic pathways, serine biosynthesis and cellular amide metabolic pathways (Fig. 3b; Extended Data Fig. 4c). Moreover, a flux balance analysis, which predicts the metabolic state of single cells[23], suggested that triacylglycerol biosynthesis and tryptophan metabolism are downregulated in GPR65-deficient Th17 and Th22 cells, respectively (Extended Data Fig. 4d).

To investigate how metabolism-related target genes are linked to GPR65 function, we closely compared the differential expression of genes related to lipid metabolism, amino acid metabolism, oxidative phosphorylation, glycolysis, ATP metabolism and cellular amide metabolism (Fig. 3c; Extended Data Fig. 5a). We identified downregulation of fatty acid metabolism (*Dgat1*, *Hilpda*, *Scd2*) and cholesterol metabolism (*Cyp51*, *Msmo1*, *Npc2*, *Hmgcr*) genes and upregulation of polyamine metabolism (*Srm*, *Sms*, *Sat1*) and serine metabolism (*Phgdh*, *Psph*, *Psat1*) genes in GPR65-deficient T cells (Fig. 3c,d; Extended Data Fig. 5b). Notably, *Fabp5*, which is related to fatty acid transport, showed higher expression and *Smox*, which encodes the spermine oxidase in polyamine metabolism, had lower expression in *Gpr65*-null cells. We further validated the differential regulation of lipid metabolism (*Dgat1*, *Fabp5, Cyp51*, *Msmo1*) and polyamine pathway (*Srm*, *Sms*, *Smox*) genes, especially in I231L-expressing Th17 and Th22 cells (Fig. 3e; Extended Data Fig. 5c). Together, these results suggest that GPR65 regulates the expression of lipid and amino acid metabolism genes in T cells, which are important for Th17 and Th22 differentiation and function.

To further define alterations in cellular metabolism in *Gpr65*-null and I231L-expressing Th cells, we applied metabolomic profiling to *in vitro* polarized Th17 and Th22 cells. The differential expression of fatty acid and cholesterol metabolism related genes led us first to perform non-targeted lipidomic profiling. We detected 160 lipid metabolites from both Th17 and Th22 cells. Remarkably, 37 and 46 out of 54 detected triacylglycerides (TAGs) were decreased in GPR65-deficient compared to WT Th17 and Th22 cells, respectively, suggesting a defect of TAG biosynthesis (Fig. 4a; Extended Data Fig. 6). This was in accordance with the downregulated expression of *Dgat1* (Fig. 3e), which encodes a key enzyme in TAG biosynthesis[24].

When applying differential analysis of the lipid metabolites from the fatty acid side chains, we found a decrease of polyunsaturated fatty acid (PUFA) in *Gpr65*-null cells (Fig. 4b), suggesting a shift in fatty acid composition with GPR65 deficiency. In particular, arachidonic acid (AA, C20:4) and linoleic acid (LA, C18:2) were reduced in *Gpr65*-null cells. We therefore examined the influences of PUFAs on Th22 differentiation and IL-22 production. Administration of AA partially rescued IL-22 deficiency in *Gpr65*-null cells (Fig. 4c); this was largely independent of the PPARγ signaling pathway, although AA is

a ligand for PPARγ[25], as PPARγ inhibition displayed a minor effect on IL-22 production (Fig. 4d). These results suggest that GPR65 might regulate Th22 polarization and function by modulating fatty acid metabolism. Previous reports demonstrated that cyclic AMP response element-binding protein (CREB) phosphorylation can directly promote IL-22 production through CREB binding sites in the *Il22* promoter[26]. Indeed, CREB inhibition abrogated the acidic pH-induced increase of IL-22 production in WT Th22 cells (Fig. 4e), indicating that IL-22 production promoted by GPR65 activation is dependent on CREB.

While the scRNA-seq results also suggested differential expression of polyamine metabolic and serine biosynthesis genes, such related metabolites had no consistent differences or were not detected in our metabolomic analysis.

GPR65 regulates lipid metabolism by the cAMP-CREB-DGAT1 axis

The decrease of PUFAs could not explain the impaired Th17 polarization of *Gpr65*-null cells, as higher levels of PUFAs inhibited IL-17A production (Fig. 4c). We therefore investigated the role of DGAT1 in Th17 differentiation. DGAT1 inhibition or loss diminished Th17 polarization and IL-17A production (Fig. 5a,b). Thus, DGAT1 deficiency was sufficient to recapitulate the impairment of IL-17A production observed in I231L and *Gpr65* KO Th17 cells (Fig. 3e). Overexpression of DGAT1 substantially rescued Th17 polarization of I231L and KO cells with a minor effect on WT cells (Fig. 5c), confirming an important role of GPR65-regulated DGAT1 expression in Th17 differentiation. CREB phosphorylation has been reported to regulate DGAT1 expression through promoter binding[27]. Indeed, we detected significantly less CREB phosphorylation in I231L and KO Th17 cells compared to WT Th17 cells (Fig. 5d). Additionally, we found that GPR65 I231L impaired acidic pH-induced cAMP increase (Fig. 5e), CREB phosphorylation (Fig. 5f) and *Dgat1* upregulation in Th cells (Fig. 5g). In order to confirm this signaling axis, we generated T cells expressing constitutively active CREB (caCREB), a fused protein of murine CREB and the VP16 transcription activation domain shown to be active independent of phosphorylation[28]. Overexpression of caCREB promoted Th17 differentiation and led to almost no differences in Th17 polarization among the three genotypes (Fig. 5h), indicating the rescue of Th17 phenotypes by increased CREB activity in *Gpr65* KO and I231L $CD4^+$ T cells. Together, these findings suggest a link between GPR65 activation and DGAT1 expression through the cAMP-CREB axis.

The changes in TAG storage and fatty acid composition induced by *Dgat1* downregulation can be linked to *de novo* fatty acid synthesis (FAS), which is crucial for Th17 differentiation and function[29, 30]. Indeed, we found decreased catalytic activity of the key enzyme in *de novo* FAS, ACC1, in I231L and KO compared to WT Th17 cells (Fig. 5i). Fatty acid turnover mediated by DGAT1 can also impact fatty acid oxidation (FAO)[24, 31]. We found lower oxygen consumption rates (OCR) in I231L and KO cells both at the basal level and under maximal respiration with extracellular palmitate supplementation (Fig. 5j–m), suggesting decreased FAO and other substrate oxidation. In addition, lower extracellular acidification rate (ECAR) in I231L and KO T cells indicated decreased basal glycolysis (Fig. 5n,o). These results suggest that GPR65 I231L restricts metabolism for energy generation and biosynthesis in Th cells.

I231L-harboring CD4$^+$ T and myeloid cells exacerbate colitis

To validate the role of GPR65 I231L in CD4$^+$ T cells during chronic colitis development, we performed the T cell transfer model, in which CD45Rb^{high} CD4$^+$ T cells sorted from mice with different *Gpr65* genotypes were transferred to *Rag1* KO recipients. In this way, we evaluated the impact of GPR65 I231L expression or GPR65 loss on CD4$^+$ T cells *in vivo*. Interestingly, we observed severe colitis phenotypes in recipients of I231L and KO T cells, including excessive body weight loss, decreased colon length and increased colon inflammation by histopathology (Extended Data Fig. 7a–c). This was consistent with elevated IFNγ levels in local colonic tissue and lower percentages of IL-17A$^+$ and IL-22$^+$ T cells in both colonic LP and mLN (Extended Data Fig. 7d–f). These cells were reported to play protective roles in CD45Rb^{high} CD4$^+$ T cell-driven colitis[32]. Thus, the data are consistent with our findings *in vitro* and demonstrate that GPR65 regulates *in vivo* Th17 and Th22 polarization and function, which is linked to colitis pathogenesis.

As GPR65 is widely expressed in various types of immune cells, we applied the T cell transfer model in the reverse direction (i.e., transfer of WT CD45RB^{high} CD4$^+$ T cells into *Rag1* KO mice with different *Gpr65* genotypes) to determine whether other cellular compartments contribute to colitis pathogenesis. Recipient G*pr65* KO and I231L mice showed severe colitis phenotypes including increased body weight loss, shorter colons and enhanced inflammation by histopathology (Fig. 6a–c). Immunophenotyping indicated increased infiltration of inflammatory monocytes, macrophages and dendritic cells as well as IFNγ$^+$ CD4$^+$ T cells in the colonic LP of I231L and KO mice (Fig. 6d; Extended Data Fig. 7g). These findings suggest that GPR65 deficiency or expression of the I231L variant in myeloid cells also adversely impacts inflammation-induced colonic injury. Consistent with this notion, increased levels of inflammatory cytokines such as IL-12, IL-23 and IFNγ were detected in the colons of *Gpr65* KO and I231L mice (Fig. 6e,f). Together, these results indicate that GPR65 dysfunction exacerbates colitis pathogenesis, with synergetic effects from various immune populations.

I231L in dendritic cells enhances antigen presentation

As a pH sensor, GPR65 activation under acidic conditions inhibits proinflammatory cytokine release from different immune cell types, such as TNF and IL-6 from macrophages and IFNγ from CD8$^+$ T cells[1, 33]. We therefore examined how GPR65 I231L influences cytokine responses in myeloid cells upon low pH stimulation. We found that GPR65 activation at pH 6.8 reduced proinflammatory cytokine TNF and IL-12/IL-23 production but increased anti-inflammatory cytokine IL-10 production in WT bone marrow-derived dendritic cells (BMDCs) after LPS stimulation (Fig. 6g). More importantly, we observed increased release of these proinflammatory cytokines by I231L and KO compared to WT BMDCs at low pH in contrast to neutral pH, where no differences were evident (Fig. 6g). These findings indicate that pH-dependent inhibition of proinflammatory cytokine release was attenuated in I231L and KO dendritic cells.

GPR65 has been shown to regulate autophagy and lysosomal homeostasis, which can directly impact antigen presentation[10, 34]. We therefore studied whether the I231L variant affects antigen uptake, processing and presentation. To this end, we employed co-culture

experiments with BMDCs and ovalbumin (OVA)-specific $CD4^+$ T (OT-II) cells incubated with different combinations of antigens and stimuli. There were mild differences in T cell activation upon stimulation by OVA peptide-loaded BMDCs with different *Gpr65* genotypes (Fig. 7a). Notably, combined with LPS stimulation or using zymosan-conjugated OVA, *Gpr65*-null and I231L-expressing BMDCs increased T cell proliferation (Fig. 7a; Extended Data Fig. 8a,b), suggesting enhanced antigen presentation. We also detected higher IFNγ production by activated T cells (Fig. 7b), which is consistent with elevated proinflammatory cytokine production in I231L and KO BMDCs. Moreover, we found higher levels of peptide-loaded mature MHC-II (pMHC-II) complex in I231L and KO BMDCs (Fig. 7c). Taken together, GPR65 exhibits anti-inflammatory roles when activated in dendritic cells: its dysfunction increases inflammatory cytokine release and enhances antigen presentation to T cells, which in turn promotes inflammatory responses.

I231L impairs lysosomal proteolysis and endo-lysosome fusion

To illuminate the mechanism by which GPR65 influences antigen presentation, we first evaluated GPR65-mediated effects on lysosomal function. Acidification is crucial for lysosomal function through the regulation of protease activity[35, 36]. We therefore used a ratiometric probe to measure pH in acidic organelles and detected a decrease of LysoSensor Yellow/Blue ratio in I231L and KO BMDCs relative to WT (Fig. 7d), indicating impaired acidification in these cells. Next, we compared the protein degradation capacity of the cells. To measure lysosomal proteolysis, we used self-quenched fluorogenic DQ-BSA and a pH insensitive Alexa Fluor 647 dye conjugated to polystyrene beads and then incubated them with BMDCs under different conditions (Fig. 7e). In both resting and LPS-activated states, I231L and KO BMDCs showed impaired DQ-BSA degradation despite similar levels of phagocytosis (Fig. 7f). We confirmed these observations of decreased DQ-BSA intensity by microscopy-based methods and observed no evident difference in Alexa Fluor 647 intensity (Extended Data Fig. 8c,d). These results suggest that the GPR65 I231L variant alters lysosomal homeostasis, impairing lysosome acidification and reducing proteolytic capacity.

The endo- or phago-lysosome fusion process is important for degradation of cargo and is delayed in mature dendritic cells, resulting in prolonged antigen retention and enhanced presentation[37, 38]. As we observed enhanced antigen presentation and decreased protein degradation in I231L and KO dendritic cells, we next evaluated whether GPR65 dysfunction affected endo-lysosomal fusion. To this end, BMDCs were incubated with either a pH insensitive fluorophore conjugated dextran or BSA to track endocytosis and monitored fusion with lysosomes labeled with LysoTracker or Lamp1 antibody. GPR65 loss or I231L expression decreased the colocalization of dextran and BSA with lysosomes, especially in activated BMDCs at low pH (Fig. 7g,h), indicating delayed endo-lysosomal fusion.

Given that pMHC-II complexes are effective stimulators of $CD4^+$ T cells, and their recycling and degradation determine antigen presentation efficiency[39], we further investigated the half-life of pMHC-II complexes in dendritic cells. BMDCs were treated with OVA peptides and then surface-biotinylated. Biotinylated pMHC-II complexes were immunoprecipitated by the Y-3P antibody specific for mature pMHC-II complexes and detected by fluorescent

streptavidin after LPS and low pH stimulation. More pMHC-II complexes were detected in I231L and KO compared to WT BMDCs (Fig. 7i), indicating a prolonged half-life of pMHC-II complexes in activated *Gpr65*-null or I231L-expressing dendritic cells. Together, these results suggest that GPR65 dysfunction alters endo-lysosomal function, sparing antigen from degradation and potentiating epitope presentation for T cell activation.

DISCUSSION

Infection or injury perturbs tissue homeostasis and initiates inflammation as a protective mechanism, which is followed by a series of events to restore homeostasis. Effective inflammation resolution requires coordinated processes involving the immune system and barrier tissues to transition from the proinflammatory state to the repair phase[40, 41, 42]. GPR65 senses acidic pH that usually occurs during inflammation, especially in the gastrointestinal tract[43, 44, 45]. The functional characterization of GPR65 I231L in the context of IBD pathogenesis illuminates how pH sensing and immune modulation impact tissue homeostasis and inflammation circuits.

Our data define the cytokine responses of both innate and adaptive immune cells at different pH. In general, GPR65 activation under acidic conditions inhibits inflammatory cytokine production but promotes anti-inflammatory cytokine release. These results suggest that GPR65 serves as a brake for inflammation during immune responses to infectious agents or injury, which is especially relevant at the later stage of tissue inflammation as the microenvironment undergoes acidification. Importantly, our study highlights the dysfunction of GPR65 I231L as a pH responder and identifies its role in colitis development at the level of immune regulation. There are at least three processes in which GPR65 I231L is involved. First, in models of inflammation *in vivo*, I231L promotes production of innate inflammatory cytokines associated with the infiltration of inflammatory myeloid cells and impairs clearance of intracellular bacteria[10]. Second, I231L impairs production of cytokines in T cells that promote tissue immunity and regeneration, such as IL-17A and IL-22, and elevates production of pathogenic inflammatory cytokines such as IFNγ. Third, in dendritic cells, I231L enhances antigen presentation to $CD4^+$ T cells through prolonged antigen display and elevated inflammatory cytokine production, which collectively promote T cell activation and polarization to inflammatory Th cells. Thus, GPR65 I231L has pleiotropic effects on different immune cell populations, which likely have synergistic effects during colitis pathogenesis.

We observe fewer IL-22- and IL-17A-producing Th cells as well as more severe disease phenotypes in both *C. rodentium* infection- and T cell-driven colitis in GPR65 I231L mice. Previous studies demonstrated a key role for GPR65 in Th17 function[46], although a molecular mechanism was not described. Here, we used scRNA-seq and metabolomic profiling to show that lipid metabolism is altered in *Gpr65*-null and I231L-expressing Th17 and Th22 cells. GPR65 dysfunction is associated with decreased expression of SCD2 and HILPDA, both reported to decrease TAGs[47, 48], as well as DGAT1, an ER-localized enzyme controlling TAG biosynthesis[24]. Impaired TAG production can diminish an important reservoir of metabolic energy and affect metabolic fluxes that support energy homeostasis and biosynthesis for cell maintenance and effector functions[24, 31, 49]. Indeed, we observe

reduced fatty acid metabolism and substrate oxidation in *Gpr65* KO cells. Our scRNA-seq data, however, indicates upregulation of oxidative phosphorylation related genes in KO cells, which might be an adaptation to the energy metabolism defect consistent with reports that a deficiency in ATP production induces compensatory upregulation of respiratory chain complexes[50, 51].

While TAG metabolism has been linked to Treg generation[52], its role in Th17 differentiation and function has not been clearly elucidated. Here, we show that pharmacologic inhibition of DGAT1 reduces IL-17A production. Moreover, phosphorylated CREB regulates *Dgat1* expression through promoter binding, and GPR65 dysfunction reduces CREB phosphorylation in I231L and KO Th17 cells. Collectively, these data suggest a model wherein GPR65 dysfunction decreases cAMP levels, suppresses the cAMP-PKA-CREB signaling axis and reduces DGAT1 expression, leading to impaired TAG metabolism in Th17 and Th22 cells.

We also found a shift of fatty acid composition by the side chain analysis of decreased TAGs in *Gpr65*-null compared to WT cells. The relative abundance of PUFA is reduced in *Gpr65*-null and I231L-expressing Th22 cells, and PUFA supplementation with arachidonic acid partially rescues the production of IL-22 but not IL-17A, consistent with reports that a subset of arachidonic acid metabolites such as prostaglandin G2 activate AhR[53]. Partially restored IL-22 production with PUFA supplementation suggests additional mechanisms underlying GPR65-dependent regulation. Indeed, the engagement of GPR65 by protons induces CREB phosphorylation, which can directly promote IL-22 production through binding to the *Il22* promoter[26]. Thus, GPR65 regulates Th22 differentiation and cytokine production via both the cAMP-PKA-CREB axis and the modulation of PUFA metabolism.

In this study, we identify a role for GPR65 in antigen presentation to $CD4^+$ T cells by dendritic cells. GPR65 I231L enhances antigen presentation through decreased protease activity and delayed endo-lysosomal fusion, which favors persistence of epitopes and increases association with MHC-II-rich compartments, thus enhancing the efficiency of antigen presentation. This is consistent with the fact that mature dendritic cells abate their antigen degradative capacity in the endo-lysosome to preserve antigenic peptides for effective activation of adaptive immune cells[34, 38, 54]. Notably, the impaired proteolytic capacity has a different impact on macrophages, which require better lysosomal degradative capacity for pathogen killing after phagocytosis[34], although limiting proteolysis in early phagosomes could similarly maximize epitope peptides for antigen presentation[55]. From this perspective, the I231L variant impairs bacterial clearance in macrophages, consistent with previous reports[10]. Moreover, GPR65 deficiency in macrophages abrogates extracellular acidification-induced inhibition of pro-inflammatory cytokines including TNF and IL-6[33], thus contributing to inflammation during bacterial infection and colitis pathogenesis.

In conclusion, we highlight the impact of a single coding variation in a pH sensor, GPR65 I231L, on tissue homeostasis and inflammation control in the context of colitis pathogenesis. Our results provide a framework to understand how immune cells sense environmental cues to modulate endo-lysosomal function and cellular metabolism in the context of inflammatory disease development. Moreover, this example of a variant-to-function study

provides key insights relevant to the development of therapeutic strategies for inflammatory pathologies.

METHODS

Mouse studies

Mouse experiments complied with all relevant ethical regulations and were performed according to protocols 2003N000158 and 2011N000126 approved by the Institutional Animal Care and Use Committee (IACUC) at Massachusetts General Hospital. C57BL/6 (JAX:000664), *Rag1* KO (JAX:002216), GPR65 (JAX:008577) and OT-II (JAX:004194) mice were obtained from the Jackson laboratory. GPR65 mice were backcrossed to C57BL/6 for over 13 generations. *Gpr65* KO or I231L mice were crossed with *Rag1* KO mice to obtain *Rag1* KO mice with different *Gpr65* genotypes. All mice were maintained in specific-pathogen free conditions and cohoused in the same room at the animal facility maintained on a 12-hour light/dark cycle with a room temperature of 21°C and relative humidity of 30–70%. Males and females 8–12 weeks old were used for mouse studies. For each genotype in each experiment, mice were age- and sex-matched. WT mice were littermates from the GPR65 and I231L lines. Number of mice used per experiment is provided in the figure legends.

GPR65 I231L mouse construction

The GPR65 I231L knock-in mouse line was constructed by CRISPR/Cas9-based systems. sgRNA target sequence (5′-TGTCGCGCTCTAAAACGCAG-3′) was screened and selected from the mouse *Gpr65* sequence prior to in vitro transcription by Guide-It sgRNA In Vitro Transcription kit (ClonTech) and purification by MEGAclear kit (Thermo Fisher). The homology-directed repair (HDR) template had a 90nt homology arm on the 5′ side of the desired mutation and a 56nt homology arm on the 3′ side of the PAM site mutation, for a total of 200nt, and was ordered from IDT and PAGE-purified. Transfection-ready Cas9 SmartNuclease mRNA was purchased from System Biosciences (CAS500A-1). Mice were generated at Harvard University's Genome Modification Facility. Mice harboring the GPR65 I231L mutation were verified by SfaNI restriction enzyme digestion (Supplementary Figure 1) and sequencing of the amplicon products with murine genomic DNA as the template (primers: 5′-CTCACTTGCATTGCCCTGGACCG-3′, 5′-CCACATATCAGCTCTCCCCGTCTC-3′). The acquired mice were backcrossed to C57BL/6 for 2 generations before use in experiments.

Citrobacter rodentium infection model

C. rodentium were grown overnight at 37°C in LB with kanamycin before being harvested and resuspended in PBS. Mice were fasted for 4h and then orally gavaged with 100μl suspension containing 1–2×10^9 colony-forming units (CFUs) of bacteria. Feces were collected on days 3, 6, 9 and 12 after infection, and colonic tissue was harvested on day 12. CFUs from feces and tissue were determined by plating homogenized suspension on LB agar with kanamycin. Distal colon (1cm) was harvested for histopathology. For *Citrobacter*-induced colitis after adoptive T cell transfer, splenic $CD4^+$ T cells were purified with the EasySep Mouse CD4+ T Cell Isolation Kit (STEMCELL). 2×10^6 $CD4^+$ T cells

were intravenously injected per *Rag1* KO recipient. *Citrobacter* infection followed at day 1 after adoptive transfer, and phenotyping was performed as above.

Immunophenotyping

Mouse colons were harvested with fat and mesenterium removed, then opened longitudinally, washed with HBSS and cut into 1cm pieces. Tissue was treated with epithelial strip buffer [5mM EDTA (Invitrogen), 1mM DTT (Sigma), 15mM HEPES (pH 7.2–7.5, Gibco) and 5% FBS (Gibco) in HBSS buffer, calcium- and magnesium-free] at 37°C for 30min with stirring, washed with HBSS and digested with enzyme digestion buffer [0.167mg/ml Liberase TL (Roche), 0.1mg/ml DNase I (Sigma) and 15mM HEPES (pH 7.2–7.5) and 5% FBS in HBSS buffer] at 37°C for 30min with stirring. The supernatant was filtered into ice-cold collection buffer (HBSS with 5% FBS and 5 mM EDTA) and harvested by centrifuge. Cell pellets were resuspended in 44% Percoll (diluted with HBSS from 100% Percoll) with carefully underlaid 67% Percoll. 50ml 100% Percoll contains 45ml Percoll (GE Healthcare), 4.48ml HBSS (10x, without calcium, magnesium or sodium bicarbonate, Sigma), 0.5 ml 1M HEPES (pH 7.2–7.5) and 0.23ml 1N HCl (Sigma). The lymphoid fractions at the Percoll interphase were collected after centrifuge at 600xg for 20min, washed with HBSS and resuspended with full RPMI 1640 medium and kept on ice. For myeloid cell analysis, cells were blocked with anti-CD16/CD32 antibody (1:100) and stained with myeloid cell panel antibodies and cell viability dye (1:1000), fixed with 2% PFA [diluted with PBS from 4% PFA (Thermo)]. For cytokine-producing cell analysis, cells were treated with 50ng/ml PMA (Sigma), 1μg/ml ionomycin (Sigma) and GolgiPlug (BD) at 37°C for 2–3h, then stained with cell viability dye and Th cell panel antibodies using Fixation/Permeabilization Solution Kit (BD) according to the manufacturer's protocol. All staining was performed in MACS buffer (PBS with 2.5mM EDTA, 2% FBS) or PBS. All flow cytometry samples were detected by NovoCyte Flow Cytometer with NovoExpress (v1.4.1) (Agilent). Data were analyzed using FlowJo (v10.7.1). Antibody information is available in Supplementary Table 1.

IL-17A ELISPOT

MultiScreen-IP Filter Plates (Millipore) were coated with mouse IL-17A capture antibody (1:200 dilution in PBS, BioLegend, 432504) overnight, washed with PBS and blocked with 2% BSA in PBS for 30min at 21°C. Cells were harvested from mesenteric lymph nodes on day 7 after *C. rodentium* infection, and single cell suspensions were prepared in full RPMI 1640 medium. Lymph node cells were plated (2.5×10^5 cells/200μl/well) and Citrobacter peptide (AAIAVNPVVSSTTDS) was added to a final concentration of 100nM or 0nM. The immunodominant Citrobacter peptide was predicted using the BOTA algorithm[56]. Cells were cultured at 37°C overnight before supernatant was collected for cytokine detection by IL-17A or IL-22 ELISA kit (BioLegend). ELISPOT plates were washed with H_2O and blocked with 2% BSA in PBS for 60min at 21°C. IL-17A detection antibody (1:200 dilution, BioLegend, 432504) and detection reagent (AKP Streptavidin 1:1000, BD) in 2% BSA were added and incubated for 1–2h at 21°C. Plates were washed with H_2O, BCIP/NBT substrate (Sigma) was added, and plates were dried for detection by CTL ImmunoSpot analyzer with ImmunoSpot 7. Data were analyzed by ImmunoSpot 7.

In vitro CD4+ T cell differentiation

Mouse splenic naïve CD4+ T cells were isolated by EasySep™ Mouse Naïve CD4+ T Cell Isolation Kit (STEMCELL). Naïve CD4+ T cells were cultured in full RPMI 1640 medium (10% heat-inactivated fetal bovine serum, GlutaMAX, penicillin-streptomycin, MEM non-essential amino acids, sodium pyruvate and 2-mercaptoethanol) and stimulated in plates coated with 1 or 2μg/ml anti-mouse CD3ε and 2μg/ml anti-mouse CD28 antibodies (1×10^5 cells/200μl/well). Cytokines were supplemented for different CD4+ T cell subsets: Th1, 20ng/ml rmIL-12p70 (Peprotech); Th2, 20ng/ml rmIL-4 (Peprotech); non-pathogenic Th17, 2.5ng/ml rmTGF-b1 (R&D Systems) and 25ng/ml rmIL-6 (Peprotech); pathogenic Th17, 20ng/ml rmIL-1b (Peprotech), 25ng/ml rmIL-6 and 20ng/ml rmIL-23 (R&D Systems); Th22, 20ng/ml rmIL-1b, 40ng/ml rmIL-6, 20ng/ml rmIL-23 and 400nM FICZ (Sigma); iTreg, 10ng/ml rmTGF-b1 and 2ng/ml IL-2. For inhibitor or metabolite treatments, DGAT1 inhibitor (A922500, Tocris, 1μM), PPARγ inhibitor (T0070907, Selleckchem, 2 μM), arachidonic acid (Sigma, 10μM) or linoleic acid (Sigma, 10μM) was added to the Th17 cell culture on day 1. Cells were harvested on day 3 for analysis by intracellular cytokine staining using Fixation/Permeabilization Solution Kit (BD) according to the manufacturer's protocol. For restimulation, cells were stimulated by 50ng/ml PMA (Sigma), 1μg/ml ionomycin (Sigma) and GolgiPlug (BD) for 3–4h, then harvested for intracellular cytokine staining. For repolarization to Th1-like cells, Th17 or Th22 cells were harvested on day 3, washed with RPMI 1640 medium, and stimulated by plate-coated anti-mouse CD3ε and CD28 antibodies with Th1 condition cytokines (20ng/ml rmIL-12p70 and 20ng/ml rmIL-23) for 24h.

T cell nucleofection

DGAT1 expression plasmid was constructed by inserting the murine *Dgat1* gene in pMSCV backbone with mRFP1 driven by the IRES sequence (#33337, Addgene). Murine caCREB expression plasmid was constructed by fusing the VP16 transcription activation domain (#42499, Addgene) at the C terminus of murine *Creb1* (#154942, Addgene) in the pCMV backbone with *Flag* tag at the N terminus of *Creb1* ORF. Purified naïve $CD4^+$ T cells were stimulated by Dynabeads Mouse T-Activator CD3/CD28 (Gibco) for 24h, then collected for nucleofection with P3 Primary Cell 4D-Nucleofector X Kit (Lonza) and program CM-137. Cells were cultured under Th17 polarization conditions for 36–40h followed by intracellular IL-17A staining and flow cytometry analysis. $mRFP1^+$ or $FLAG^+$ cells were gated to compare $IL\text{-}17A^+$ cells between genotypes.

Cytokine detection

For cytokine detection from murine colonic tissue, 1cm distal colon was harvested and homogenized in PBS by TissueLyser LT. Supernatant was collected for use with LEGENDplex™ Mouse Inflammation Panel (BioLegend) and ELISA MAX™ Deluxe Set Mouse IL-22 kit (BioLegend). For T cell cytokine detection at different pH, *in vitro* polarized Th cells were harvested on day 3 and rested for 24h before restimulation by plate-coated anti-mouse CD3ε and anti-mouse CD28 (2μg/ml each) in full RPMI 1640 medium with different pH adjusted by 1N HCl (Sigma). CREB inhibitor (666–15, Selleckchem, 100nM) was used for inhibition in Th22 cells. Culture supernatants were collected after

24h stimulation, and cytokines were detected by Deluxe Set Mouse IL-17A, IFNγ, IL-22 and TNF ELISA kits (BioLegend). For myeloid cell cytokine detection at different pH, BMDCs were harvested on day 7 after 20ng/ml GM-CSF (PeproTech) induction, then stimulated by 20ng/ml LPS in full RPMI 1640 medium with different pH adjusted by 1N HCl. Culture supernatants were collected after 4h (TNF and IL-12p40) or 24h (IL-10) stimulation, and cytokines were detected by Deluxe Set Mouse TNF, IL-12p40 and IL-10 ELISA kits (BioLegend).

Single-cell RNA-sequencing

In vitro polarized Th17 and Th22 cells were prepared as above. Cells were harvested on day 3, validated for effective polarization and submitted for 10x genomics single-cell RNA-sequencing. In total, 8 libraries were prepared, with 2 replicates of each combination of genotype (KO, WT) and polarization condition (Th17, Th22).

Single-cell data analysis

Data processing and QC: Digital gene expression (DGE) matrices for each individual sample were obtained by aligning FASTQ sequence reads to the reference mm10 mouse transcriptome using CellRanger v5.0.1 (10x Genomics). Removal of cells with background or ambient RNA was done by processing the raw DGE matrix through CellBender (v0.2.0) package[57]. The filtered DGE count matrices of cell X UMI barcodes was processed, and poor-quality cells were identified and removed based on the following exclusion criteria: 1) cells with <200 detected genes; 2) cells having outlier number of unique molecular identifiers (UMIs) >10,000; 3) cells having outlier number of identified genes >3000; and 4) proportion of mitochondrial gene expression >10%. This removed 5.9% of cells, leaving 104,660 cells for downstream analyses.

Normalization and integration: DGE matrices of each individual sample were merged and read-depth normalized using standard logTP10K normalization. Top 500 variable genes were identified using a LOESS regression method with the *FindVariableFeatures* in Seurat (v4.1.0). The normalized expression matrix was centered and adjusted for cell cycle scores (S phase and G2M phase) + nUMI + % mitochondrial gene expression. Principal component analysis was conducted on the residual scaled expression matrix, and top 30 eigenvectors explaining a substantial proportion of variance were considered for downstream analysis based on inspection of the elbow plot. Integration of sample-specific data was performed using the Harmony algorithm[58], implemented by the *RunHarmony* function in Seurat (v4.1.0), by considering each individual library as a separate batch.

Clustering and visualization: Harmony-corrected loadings were used for construction of a k-NN graph using the *FindNeighbors* function (*nn.method*=rann, *nn.eps*=0.25, *k.param*=130 and *dims*=1:30). Subsequently the Louvain clustering algorithm was applied using *FindClusters* (*method*=matrix, *n.start*=10, *resolution*=0.4). Resulting clusters were visualized in the Uniform Manifold Approximation and Projection (UMAP) embedding space.

Differential expression analysis: We used the MAST method, which fits a hurdle model to the normalized expression levels for each gene, to identify differentially expressed genes between any two conditions. We compared gene expression levels from cells identified in a given cluster with all the set of cells in the complement group (*e.g.* WT Th17 vs. KO Th17 for cluster 3).

Flux balance analysis

We inferred single-cell level metabolic state from single-cell transcriptome profiles using Compass (v0.9.10.2)[59], a Flux Balance Analysis-based algorithm[23] that utilizes prior knowledge of the metabolic network consisting of metabolic reactions, enzymes, stoichiometry and biochemical constraints. Compass estimates flux through the network of metabolic reactions, taking into input the observed expression levels of enzyme-coding transcripts in each cell.

We applied Compass to our scRNA-seq data, which was subset to have a maximum 2,500 cells for each cluster. The total size of the subset data was 24,420 single cells with >2,300 cells/sample. In total, we estimated scores for 6,410 metabolic reactions in >24,000 cells. We compared the difference between metabolic states of cells between any two conditions for each cluster by applying Wilcoxon's rank sum test for estimated reaction scores and Cohen's D test to estimate the effect size.

Lipidomics and metabolomics

In vitro polarized Th17 and Th22 cells were prepared as above. Cells were harvested on day 3, washed with PBS and pellets were snap frozen and stored at −80°C before treatment for detection. Cell profiling was performed leveraging liquid chromatography-tandem mass spectrometry (LC-MS/MS) method[21]. A C8-positive platform, which connected a Nexera X2 U-HPLC (Shimadzu Corp) to an Exactive Plus orbitrap mass spectrometer (Thermo Fisher Scientific), was used to measure polar and non-polar plasma lipids. Internal standard peak areas were monitored for quality control and to ensure system performance throughout analyses. Pooled Th17 and Th22 reference samples were inserted every 20 samples as an additional quality control. Untargeted data were processed using Progenesis QI software (Waters, Milford, MA) and TraceFinder 3.1 (Thermo Fisher Scientific, Waltham, MA) for automated LC-MS peak integration.

Dgat1 knockout

Dgat1 knockout in murine $CD4^+$ T cells was performed by CRISPR-Cas9 ribonucleoproteins (RNPs) transfection[60]. Briefly, murine *Dgat1*-targeting guide RNAs were designed by IDT and selected (5'-CCACCTGGATAGGATCCACC-3'). crRNA and tracrRNA oligos (IDT, 120μM) were annealed at 1:1 mole ratio by heating at 95°C for 5min and slowly cooled to 21°C, then gently mixed with Cas9 protein (PNA Bio, 30μM) at equal volumes followed by incubation at 37°C for 15min to form RNPs. Purified naïve $CD4^+$ T cells were activated by plate-coated anti-CD3ε and anti-CD28 (2μg/ml each) antibodies for 24h. 4×10^5 cells were collected and resuspended in 20μl primary cell nucleofection solution (P3 primary cell buffer, Lonza) with 2μl RNPs. Nucleofection was performed with program CM-137. Cells were rested for 16h, then cultured under Th17 polarization condition for 3

days. For intracellular staining of DGAT1 and cytokines, cells were fixed and permeabilized with BD Cytofix/Cytoperm Fixation/Permeabilization Solution Kit for 20min, blocked with 2% BSA for 30min, then stained with DGAT1 (Abcam, ab181180, 1:400) and IL-17A antibodies (1:150) in Perm/Wash buffer with 2% FBS for 30min followed by Alexa fluor 647 goat anti-rabbit IgG antibody (1:1000) for 30min. After washing, cells were detected by flow cytometry.

cAMP detection

cAMP was detected in T cells using LANCE Ultra cAMP kit (PerkinElmer) according to the manufacturer's protocol. Briefly, T cells were harvested after 24h stimulation by 2μg/ml anti-mouse CD3ε/CD28 and resuspended at 2×10^6 cells/ml in RPMI 1640 medium (20mM HEPES, 0.1% BSA and 0.5mM IBMX) with neutral or low (6.8) pH adjusted by 1N HCl. Cells were transferred to white opaque 384-well microplates (20μl/well) and stimulated at 37°C for 30min. 5μl/well Eu-cAMP tracer (1:33) followed by 5μl/well anti-cAMP antibody (1:100) was added to each well. The plate was incubated at 21°C in the dark for 1h before fluorescence was detected using SpectraMax M5 multi-mode microplate reader with SoftMax Pro6 (v6.2.1). Data were analyzed by GraphPad Prism (v8.0.2).

ACC1 activity detection

ACC1 activity was determined using the acetyl-CoA carboxylase microplate assay kit (MyBioSource, MBS8303295) according to the manual. Briefly, day 3 polarized Th17 cells were harvested, resuspended in assay buffer at 2.5×10^6 cells/ml, and sonicated with power 20%, sonication 3s, interval 10s for 25 cycles. Supernatant was collected after centrifuge for detection. Absorbance at 635nm was measured by SpectraMax M5 multi-mode microplate reader with SoftMax Pro6 (v6.2.1). Data were analyzed by GraphPad Prism (v8.0.2).

CREB phosphorylation detection

For phospho-CREB detection by phospho-flow cytometry, 2×10^5 *in vitro* polarized Th17 cells were harvested on day 3, then fixed and permeabilized by BD Fixation/Permeabilization Solution Kit. After washing, cells were stained with phospho-CREB (Ser133) (87G3) rabbit antibody (Cell Signaling, 1:400) at 21°C for 1h, then stained with AF647 goat anti-rabbit IgG antibody (1:1000) at 21°C in the dark for 1h. After washing, cells were resuspended in PBS and detected by flow cytometry. Data were analyzed using FlowJo (v10.7.1).

Substrate oxidation detection

Substrate oxidation detection was performed using Agilent Seahorse XFe96 analyzers according to the manufacturer's instructions. Briefly, cells were harvested and treated in substrate-limited growth media (Seahorse XF RPMI Medium, pH 6.8 with 1% FBS, 0.5 mM glucose, 1 mM glutamine and 0.5mM L-carnitine) for 18h, then changed to assay medium (Seahorse XF RPMI Medium, pH 7.4 with 2 mM glucose, and 0.5mM L-carnitine) and loaded in plates precoated with 0.015% poly-L-lysine at 1×10^5 cells/well. Etomoxir (4μM) was added for 20min before palmitate was added for oxidation detection. Samples were mixed (3min) and measured (3min). Oligomycin (1.5μM), carbonyl

cyanide-4-(trifluoromethoxy) phenylhydrazone (1.5μM), and rotenone/antimycin (0.5μM) were injected at the indicated time points. Data were analyzed by Agilent Seahorse Analytics (2.6.1.56).

CD45RB^{high} CD4+ T cell transfer model

Splenocytes were harvested from donor mice, and CD4+ T cells were enriched using EasySep™ Mouse CD4+ T Cell Isolation Kit (STEMCELL). Cells were blocked with anti-CD16/CD32 antibodies (1:100) and stained with anti-mouse CD4 (1:200) and anti-mouse CD45RB (1:150) antibodies in MACS buffer at 4°C for 20min. After washing, cells were resuspended in MACS buffer with 7-AAD (BioLegend, 1:50) for sorting by BD FACSAria II with FACS Diva 6.1. The highest 40% of CD4+ CD45RB+ cells (CD45RB^{high}) were sorted and resuspended at 2.5×10^6 cells/ml in PBS. 5×10^5 CD45RB^{high} T cells were intraperitoneally injected per mouse. Mice were monitored weekly by weight and euthanized for phenotyping in week 8. Distal colon (1cm) was harvested for histopathology.

Antigen presentation assay

BMDCs were prepared from bone marrow cells by culturing with 20ng/ml GM-CSF (Peprotech) for 7 days. OVA-specific naïve CD4+ T cells were purified from splenocytes of OT-II mice with EasySep™ Mouse Naïve CD4+ T Cell Isolation Kit (STEMCELL). T cells were stained with CellTrace™ Far Red cell proliferation dye (Invitrogen) following manufacturer's instructions. 2.5×10^4 BMDCs and 5×10^4 purified CD4+ T cells were mixed in full RPMI 1640 medium (200μl/well) with 100nM OVA 323–339 peptide (ISQAVHAAHAEINEAGR) or indicated amount of zymosan-conjugated OVA protein and 1mM aminoguanidine hemisulfate. After 3 days co-culturing, supernatants were assayed for IL-17A, IFNγ, IL-22 and IL-2. Cells were harvested for proliferation (T cells) or surface expression of CD86 and pMHC-II (BMDCs) analysis by flow cytometry. To prepare zymosan-conjugated OVA, 20mg/ml zymosan (InvivoGen) was incubated in 8% glutaraldehyde (Sigma) for 1h, then conjugated with 1mg/ml ovalbumin for 1h at 21°C.

Lysosomal pH detection

BMDCs were harvested on day 7 after 20ng/ml GM-CSF induction. Conditions were untreated, treated with 20nM bafilomycin A1 or incubated in low (6.8) pH RPMI 1640 adjusted by 1N HCl for 2h. Cells were then stained with 1μM LysoSensor™ Yellow/Blue DND-160 (Invitrogen) in culture medium at 37°C for 5min, washed and resuspended in PBS with 7-AAD (1:50) for flow analysis by BD LSR II with FACS Diva 6.1.

DQ-BSA degradation assay

Polybead® Amino Microspheres (3.00μm, Polysciences) were conjugated with DQ-BSA and Alexa Fluor 647 by first treating with 8% glutaraldehyde in PBS at 21°C overnight with rotation. Polybeads were then incubated with 100μg DQ Red-BSA protein (Invitrogen) for 3h. After washing, polybeads were conjugated with 2μl Alexa Fluor 647 NHS ester dye (10mg/ml) in 200μl 0.1M $NaHCO_3$ buffer at 21°C for 3h. Polybeads were resuspended in original volume of PBS for later use. BMDCs were harvested on day 7 after GM-CSF induction and seeded at 0.5×10^5 cells/well in 96-U bottom plates. BMDCs were untreated or

treated with 20nM bafilomycin A1 or 20ng/ml LPS in full RPMI 1640 medium with neutral or acidic (6.8) pH for 2h. DQ-Red BSA and AF647 conjugated polybeads were then added at ratio of 10:1 (beads:cells) for 1h. BMDCs were harvested and stained with cell viability dye and anti-mouse CD11c antibody (1:100) for flow cytometry detection.

For microscopy-based detection, BMDCs were treated as above, then 3μg/ml AF647-BSA and 3μg/ml DQ-Red BSA were added for 1h. Cells were washed, fixed for DAPI staining, imaged with ImageXpress Micro confocal microscope with MetaXpress (v6.2.3), and processed and analyzed using Image J (v1.53, NIH, USA) and Image Pro Plus (v6.0, Media Cybernetics).

Endo-lysosome fusion assay

BMDCs were harvested on day 7 after GM-CSF induction, seeded in chamber slides (Thermo Scientific) and rested overnight. BMDCs were incubated with 50μg/ml AF647-dextran for 1h or 50μg/ml AF594-BSA for 2h and then untreated or treated with 20ng/ml LPS in full RPMI 1640 medium with neutral or acidic (6.8) pH at 37°C for 1–2h. After washing, AF647-dextran treated cells were stained with Lysotracker Red DND-99 (Invitrogen) at 37°C for 10min, fixed in 2% PFA at 21°C for 10min and stained with DAPI for imaging. AF594-BSA treated cells were fixed in 4% PFA at 21°C for 20min, blocked with 2% BSA in PBS with 0.1% Triton X-100 for 1h then stained with anti-mouse LAMP1-AF647 antibody (BioLegend, 1:150) in PBS with 0.1% TritonX-100 for 1h. After washing, cells were stained with DAPI. Images were captured with Nikon A1R confocal microscope with NIS-Elements AR (v5.21), then processed and analyzed using Image J (v1.53) and Image Pro Plus (v6.0).

pMHC-II complex half-life assay

BMDCs were incubated with 100nM OT-II peptide for 2h and biotinylated with 1mM NHS-Biotin (Sigma) in PBS (pH8.0) at 10×10^6 cells/ml at 21°C for 30min. Cells were washed with 25mM glycine in PBS and kept in full RPMI 1640 medium for 30min. Biotinylated BMDCs were unstimulated or stimulated with 20ng/ml LPS in full RPMI 1640 medium with low (6.8) pH for 4h. 2×10^6 cells were harvested and lysed in RIPA buffer on ice for 20min. Cell lysis supernatant was used for immunoprecipitation with 40μl protein A/G magnetic beads (Millipore) and 4μg anti-mouse MHC-II Y-3P antibody (BioXcell). Beads were stained with streptavidin-AF647 and detected by flow cytometry. Data were analyzed by FlowJo (v10.7.1).

qPCR

Colonic tissue was homogenized with TissueLyser LT. RNA was extracted from tissue or cells using RNeasy Plus Mini Kit (Qiagen) and reverse-transcribed using iScript cDNA Synthesis kit (Bio-Rad). Relative mRNA levels were detected using iTaq Universal SYBR Green Supermix (Bio-Rad) and quantified with the ΔΔCt method using *Gapdh* or *Actb* as the internal control. qPCR was run on a CF384 Real-Time system (C1000 Touch Thermal Cycler) with Bio-Rad CFX Manager 3.1. qPCR primer sequences are provided in Supplementary Table 2.

Statistics

Data were analyzed in GraphPad Prism 8 (v8.0.2). Data distribution was presumed to be normal but this was not formally tested. Statistical analyses were performed as indicated in the legends. Sample sizes and P values are provided in the figures. No statistical methods were used to pre-determine sample sizes, but our sample sizes are similar to those previously reported[10, 21, 32] and provided sufficient power for statistical analysis. All error bars represent standard error of the mean (SEM), and bars represent mean in all scatter plots with bar. No data were excluded from the analyses. Mice were randomly assigned to experimental groups where applicable. Data collection and analysis were performed in a blinded manner whenever possible. Data analysis was not blinded for experiments grouped by genotype due to the experimental design, but unbiased quantification were applied to obtain the results. Blinding was performed for lipidomic data collection, and investigators were blinded to group allocation.

Extended Data

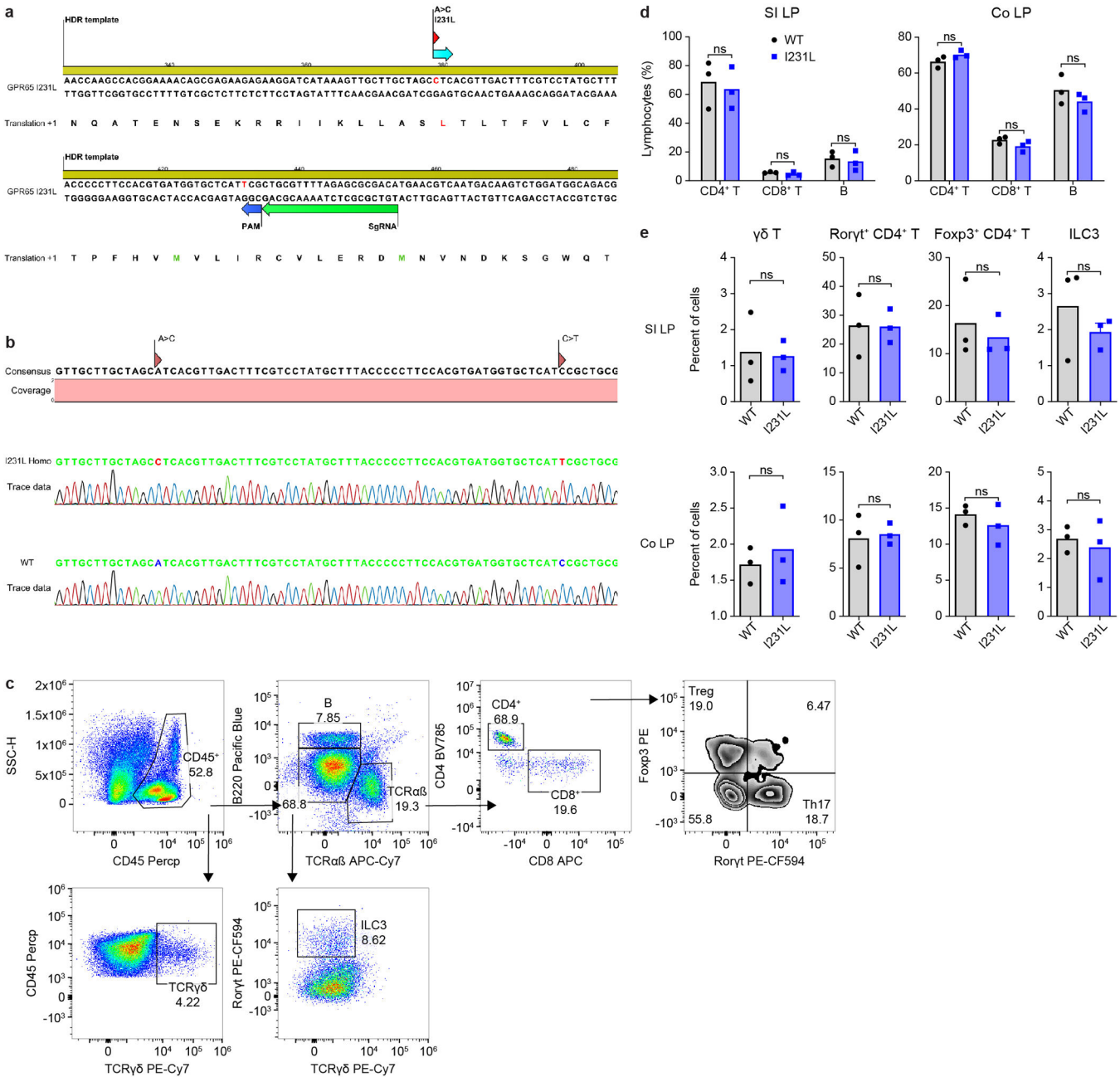

Extended Data Figure 1. GPR65 I231L mice generated by CRISPR-Cas9 have no evident colitis-related phenotypes at steady state.

(a) Design of GPR65 I231L knock-in by the CRISPR-Cas9 system. *Gpr65* gene sequence from NCBI database is shown with annotated sgRNA target sequences and protospacer adjacent motif (PAM) and mutation sites. Mutated alleles are highlighted. **(b)** Alignment of the sequencing data of WT and I231L mice. Mutated alleles are highlighted. **(c)** Gating strategy of immune populations in the small intestinal lamina propria. **(d,e)** Statistical analysis of immune populations in the small intestinal lamina propria (SI LP) and colonic

lamina propria (Co LP) of WT (n=3) and I231L (n=3) mice. Data are mean values. P values determined by unpaired two-tailed t-test; ns, not significant.

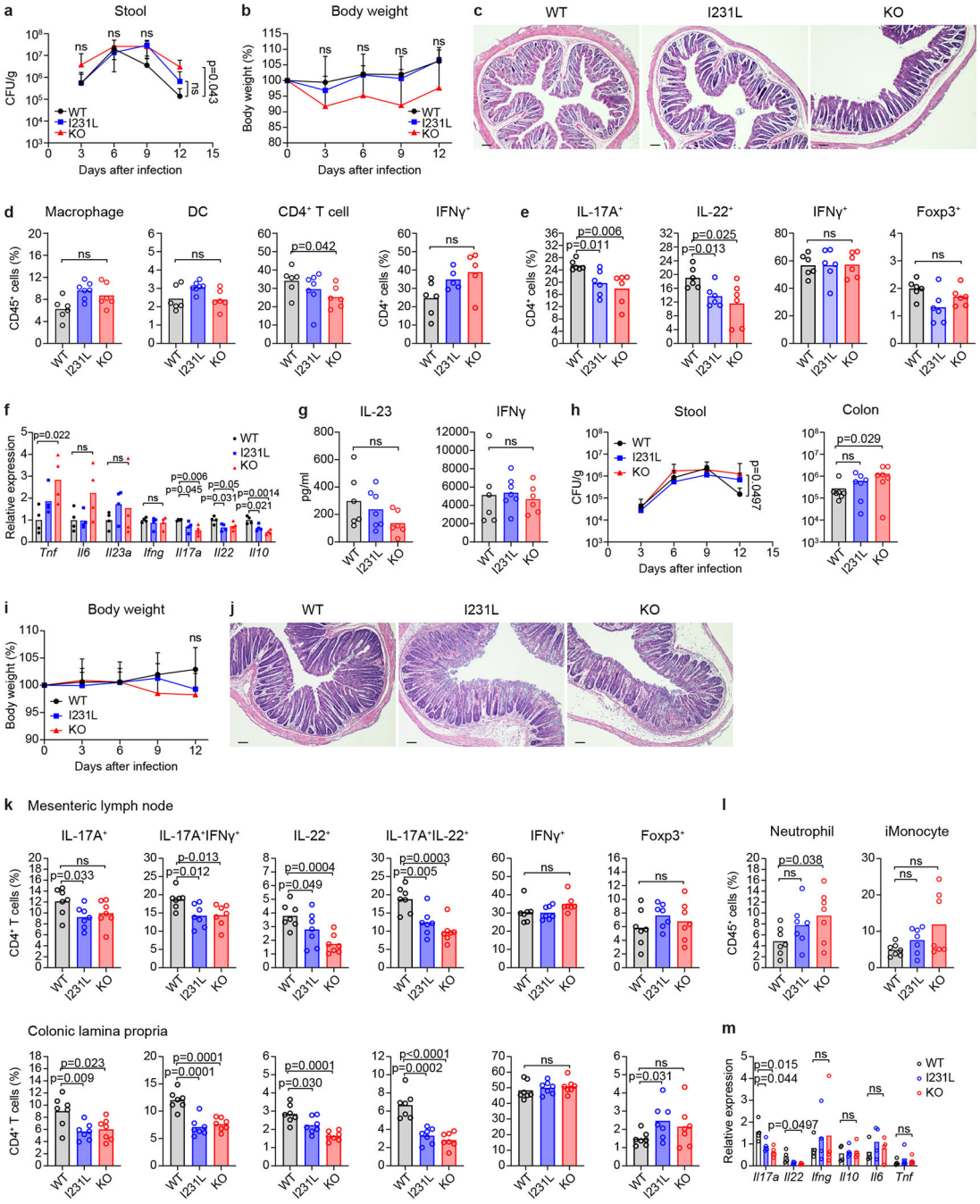

Extended Data Figure 2. GPR65 I231L mice are more susceptible to bacterial infection-induced colitis.

(a,b) Colony forming units (CFU) in the stool (a) and body weight changes (b) of mice during *C. rodentium* infection. n_{WT}=6; n_{I231L}=7; n_{KO}=6 mice. **(c)** H&E-stained sections of distal colon from mice on day 3 after *Citrobacter* infection. Representative images from one of two independent experiments. Scale bar, 0.5mm. **(d)** Statistical analysis of myeloid and

$CD4^+$ T cells in the colonic LP on day 12 after *C. rodentium* infection. $n_{WT}=6$; $n_{I231L}=7$; $n_{KO}=6$ mice. **(e)** Cytokine producing $CD4^+$ T cells in the mLN from WT (n=6), I231L (n=6) and KO (n=6) mice on day 12 after infection. **(f,g)** Cytokine profiles of colonic tissue from *C. rodentium*-infected mice detected by qPCR (f) and multiplex bead-based cytokine assay (g). n=4 mice per genotype (f); $n_{WT}=6$; $n_{I231L}=7$; $n_{KO}=6$ mice (g). **(h-j)** CFU, body weight change and colonic H&E histology of WT (n=7), I231L (n=7) or KO (n=7) $CD4^+$ T cell-transferred mice after *Citrobacter* infection. CFUs in colon tissue and H&E staining were performed on day 12. **(k,l)** Immunophenotyping of $CD4^+$ T cells and inflammatory innate immune cells in the mLN or colon LP on day 12 after infection. n=7 mice per genotype. **(m)** Cytokine profiles of colonic tissue on day 12 were detected by qPCR. n=4 mice per genotype. Scale bar, 0.5mm (c,j). Data represent at least two independent experiments. Data are mean values (a,b,d-i,k-m) + SEM (a,b,h,i). P values determined by unpaired two-tailed t-test; ns, not significant.

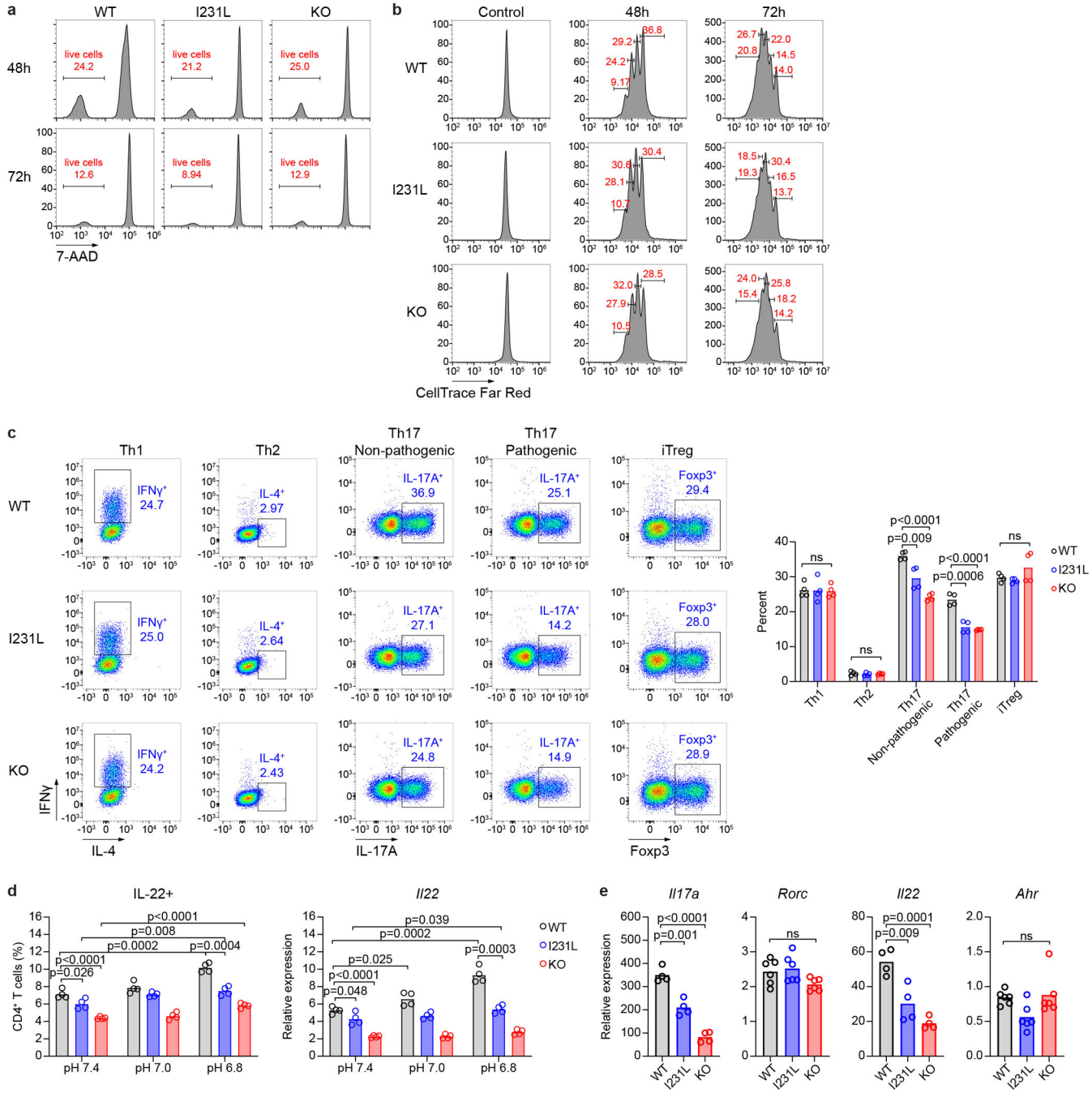

Extended Data Figure 3. GPR65 regulates Th17 differentiation.

(a) Flow profiles of cell viability of CD4$^+$ T cells after 48h and 72h of *ex vivo* culturing without stimulation. **(b)** Flow profiles of divided CD4$^+$ T cells after 48h and 72h of stimulation with anti-CD3/CD28 dynabeads. **(c)** *In vitro* polarization of different Th cells (Th1, Th2, non-pathogenic Th17, pathogenic Th17) and induced Tregs. **(d)** Cytokine responses to different pH stimulation in Th22 cells polarized *in vitro*. Intracellular cytokine staining and qPCR were performed after restimulation of resting day 3-polarized Th22 cells by anti-CD3ε and anti-CD28 antibodies for 24h. **(e)** *Il17a* and *Rorc* expression in polarized

Th17 cells and *Il22* and *Ahr* expression in polarized Th22 cells detected by qPCR. Data are mean values (c-e). n=4 biological replicates for each group (c-e). P values determined by unpaired two-tailed t-test; ns, not significant. Data represent at least two independent experiments.

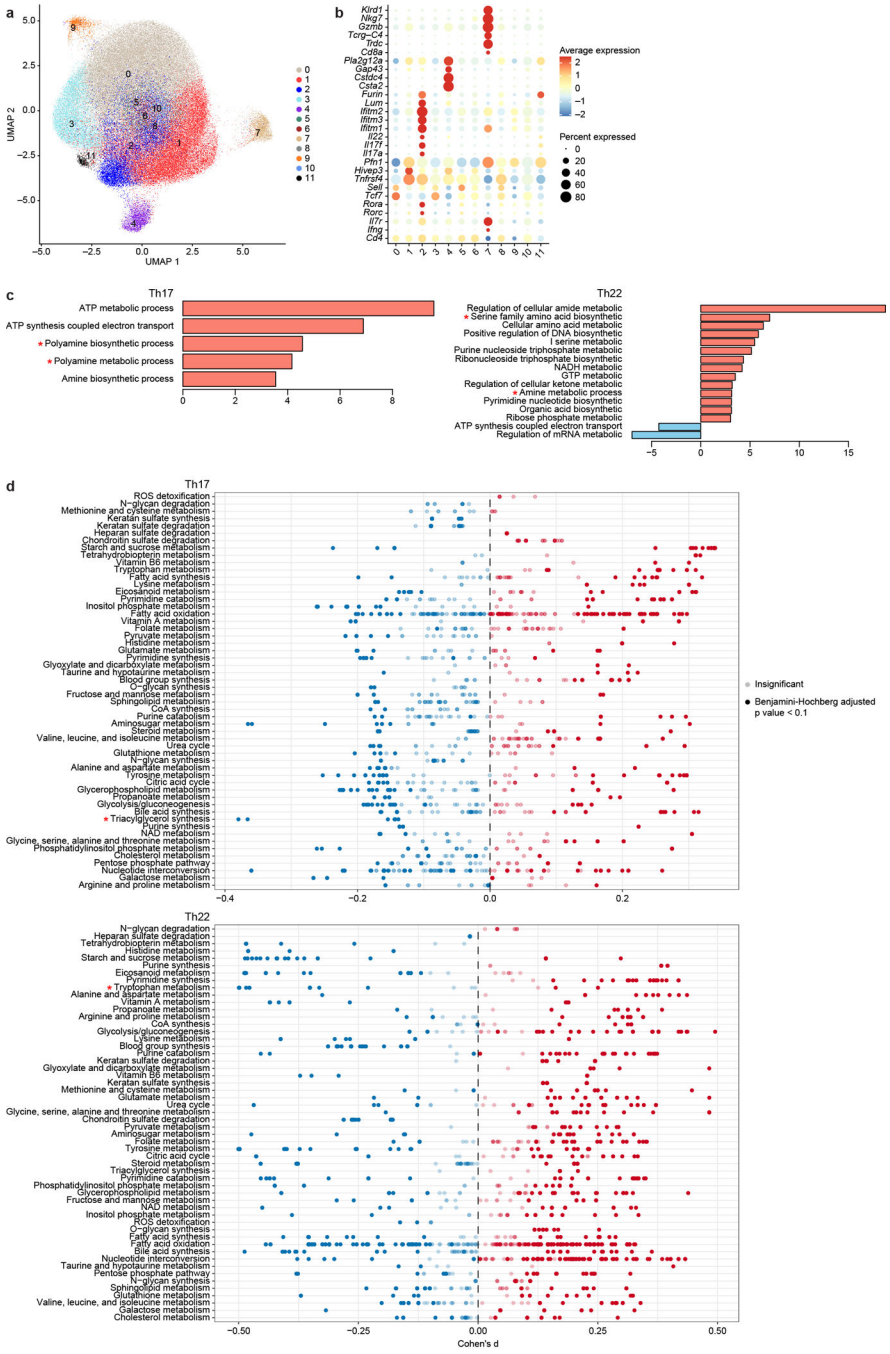

Extended Data Figure 4. Single-cell RNA-seq profiling in *in vitro* polarized Th17 and Th22 cells.
(a,b) UMAP embeddings of single-cell RNA-sequencing profiles from *in vitro* polarized Th17 and Th22 cells (a). Expression of differential genes across cells reveal the features

of different clusters (b). **(c)** Enrichment of gene ontology metabolic signature scores in cluster 2 single-cell transcriptomes for Th17 and Th22. **(d)** Flux balance analysis to predict activity of various metabolic processes. Dots denote single biochemical reactions in different metabolisms, and only core biochemical reactions are shown.

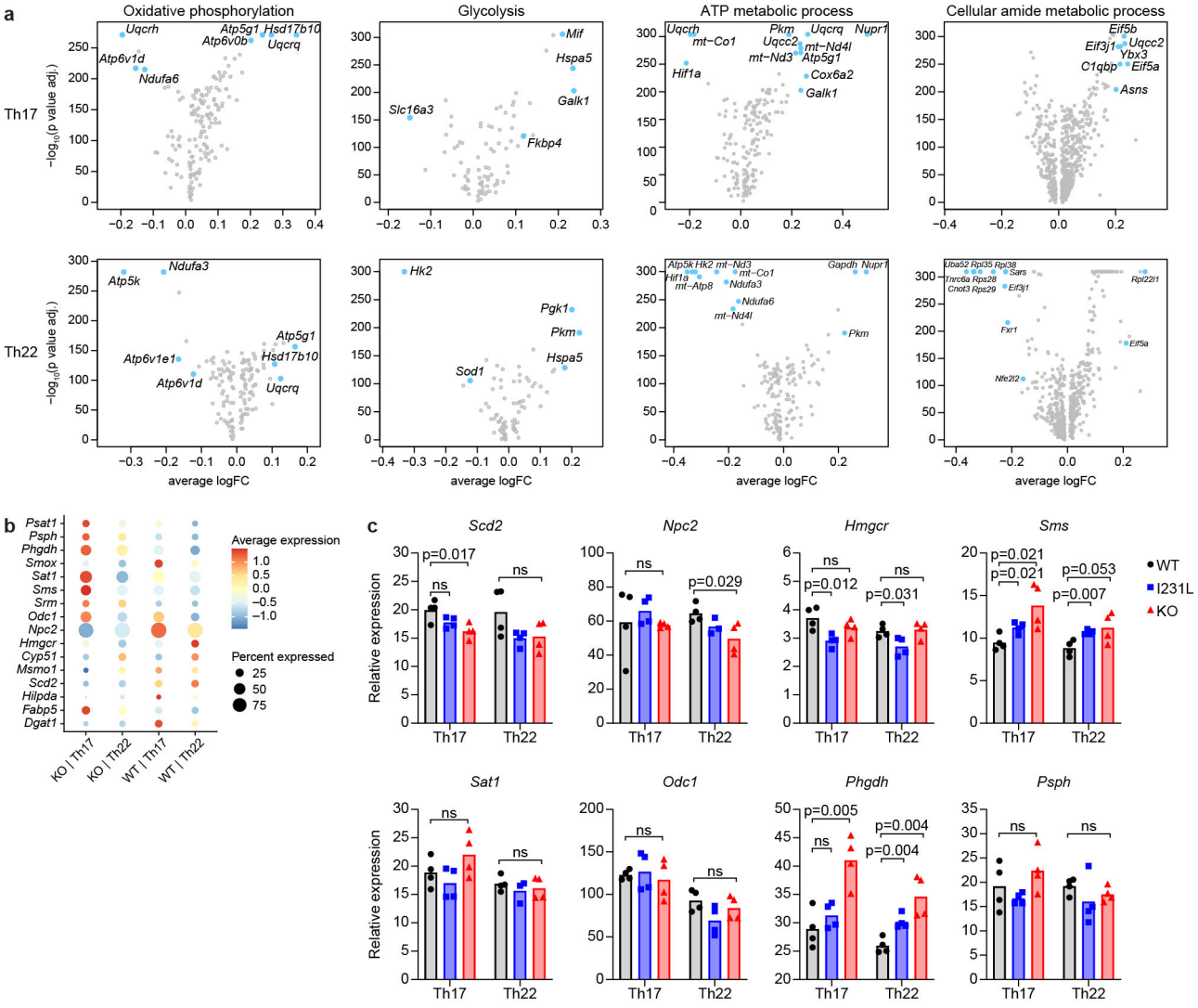

Extended Data Figure 5. Differential expression of genes related to metabolic pathways.

(a) Volcano plots show differential expression of genes related to oxidative phosphorylation (HALLMARK_OXIDATIVE_PHOSPHORYLATION), glycolysis (HALLMARK_GLYCOLYSIS), ATP metabolic process (GO_ATP_METABOLIC_PROCESS) and cellular amide metabolic process (GO_CELLULAR_AMIDE_METABOLIC_PROCESS) in polarized Th17 and Th22 cells (KO versus WT). **(b)** Dot plot shows the differential expression of genes related to different metabolic processes in all single-cell transcriptomes. **(c)** qPCR validation of differential gene expression in I231L Th17 and Th22 cells. Data are mean values from two independent

experiments. n=4 biological replicates for each group. P values determined by unpaired two-tailed t-test; ns, not significant.

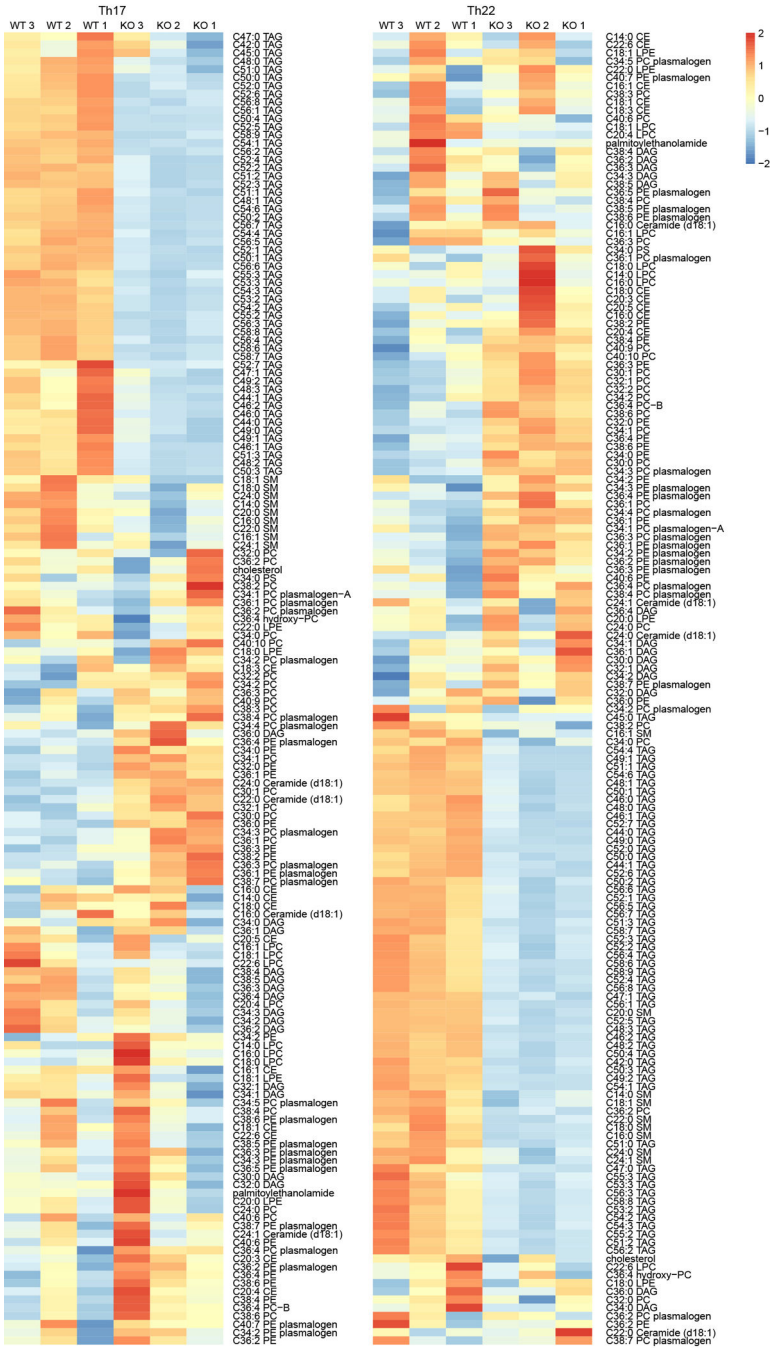

Extended Data Figure 6. Metabolomics analysis in polarized Th17 and Th22 cells.
Heatmap shows all 160 lipid metabolites detected in lipidomics.

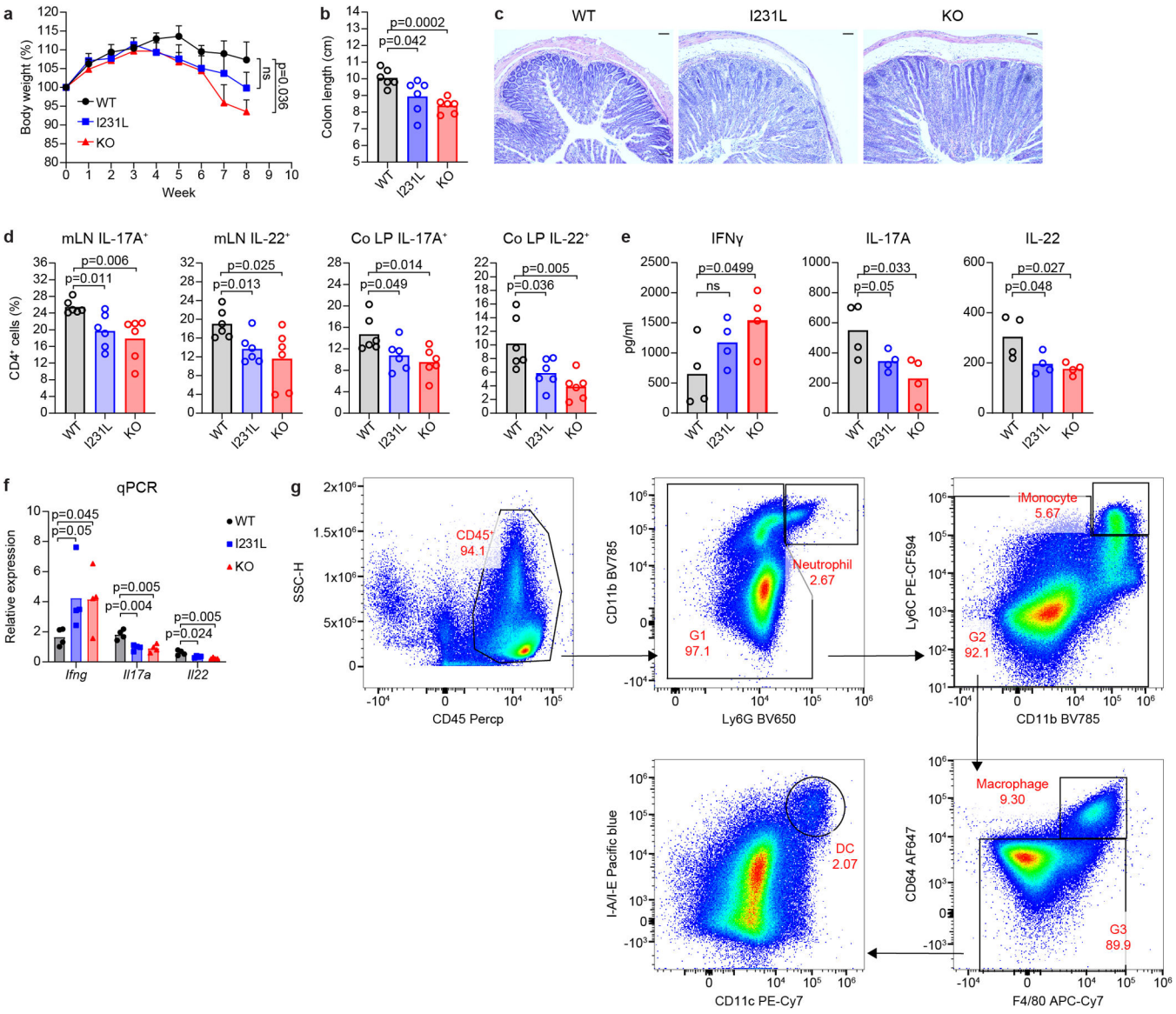

Extended Data Figure 7. GPR65 I231L exacerbates T cell-driven colitis.

(a) Body weight changes of *Rag1* KO mice after transfer of *Gpr65* WT, I231L or KO (n=6 per genotype) CD45RB^{high} CD4^{+} T cells. **(b)** Colon length of mice (n=6 per genotype) in (a) after colitis induction. **(c)** H&E-stained sections of distal colon from mice with T cell-driven colitis. Representative images from one of two independent experiments. Scale bar, 0.5mm. **(d)** Proportion analysis of cytokine producing CD4^{+} T cells in mLN and colonic LP of mice (n=6 per genotype) in (a) after colitis induction. **(e)** Cytokine profiles (IFN**γ**, IL-17A, IL-22) of colonic tissue from mice (n=4 per genotype) with colitis detected by multiplex bead-based cytokine assay. **(f)** Cytokine profiles (IFN**γ**, IL-17A, IL-22) of colonic tissue from mice (n=4 per genotype) with T cell-driven colitis detected by qPCR. One dot denotes one biological replicate (d-f). **(G)** Gating strategy of immune populations in the colonic lamina propria. Data are mean values (a,b,d-f) + SEM (a). P values determined

by unpaired two-tailed t-test; ns, not significant. Data represent at least two independent experiments.

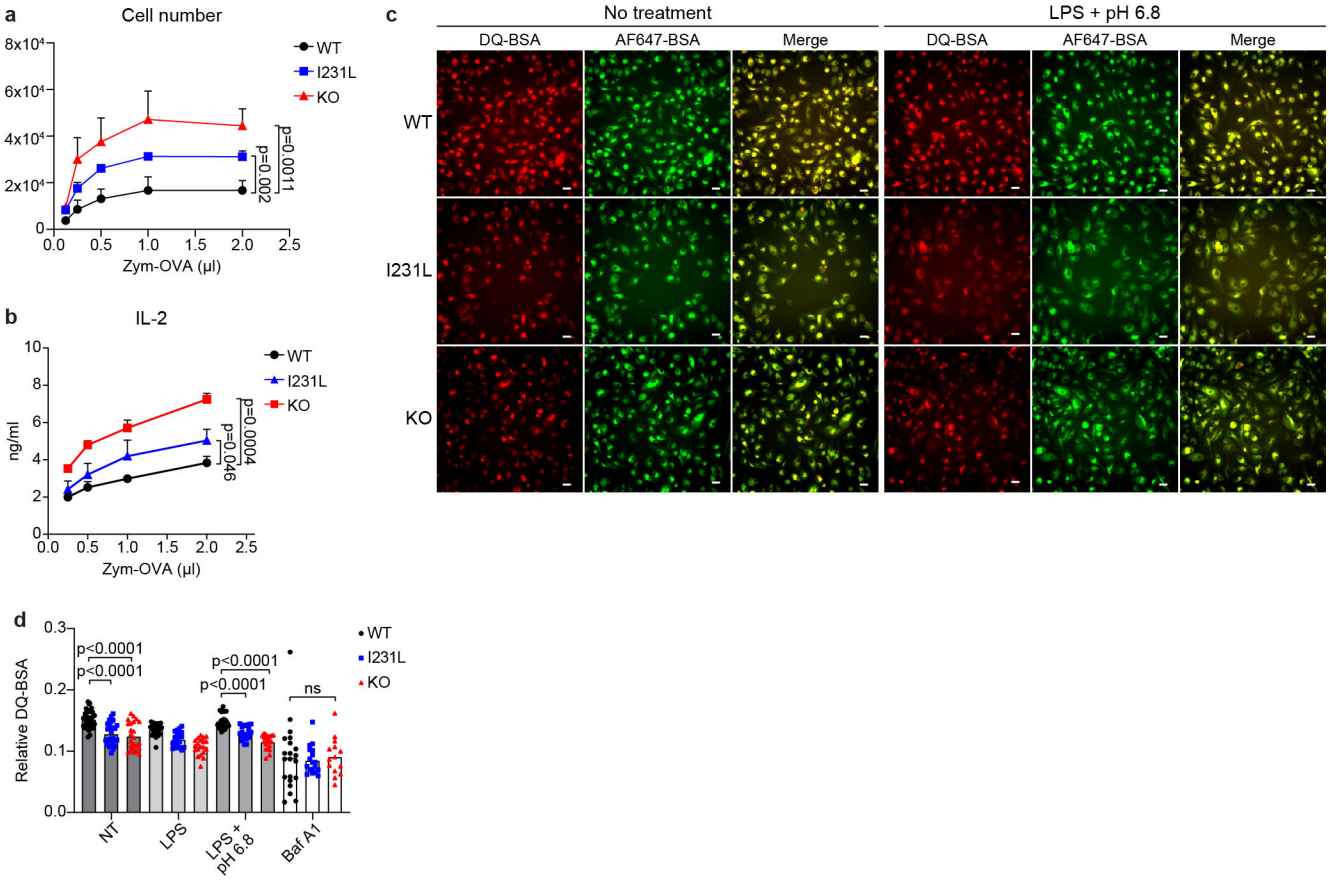

Extended Data Figure 8. GPR65 I231L enhances antigen presentation to CD4$^+$ T cell by dendritic cells.

(a,b) BMDC:OT-II T cell co-culturing-based antigen presentation assay. Cell numbers of OT-II CD4$^+$ T cells (a) and IL-2 cytokine in the culture supernatant (b) on day 3 after co-culturing are shown. n=5 (WT), n=3 (I231L) and n=2 (KO) biological replicates (a); n=4 for each group (b). **(c,d)** BMDCs incubated with both DQ-Red BSA and AF647-BSA with or without treatment. Cells were treated with LPS (20ng/ml) for 2h and then incubated with DQ-Red BSA (3μg/ml) and AF647-BSA (3μg/ml) for 1h before imaging. Representative images from one of two independent experiments are shown (c). Scale bar, 10μm. Statistical analysis of the ratio of DQ-Red BSA and AF647 fluorescence intensity (d). n_{WT}=39, n_{I231L}=28, n_{KO}=24 (NT); n_{WT}=27, n_{I231L}=20, n_{KO}=20 (LPS); n_{WT}=26, n_{I231L}=19, n_{KO}=20 (LPS+pH6.8); n_{WT}=21, n_{I231L}=18, n_{KO}=14 (Baf A1) cells. Data are mean values (a,b,d) + SEM (a,b). P values determined by unpaired two-tailed t-test; ns, not significant. Data represent at least two independent experiments.

Supplementary Material

Refer to Web version on PubMed Central for supplementary material.

ACKNOWLEDGMENTS

We thank Theresa Reimels for assistance with editing. This work was supported by funding from the National Institutes of Health (R01 DK117263, RC2 DK114784, U19 AI109725, and U19 AI142784 to R.J.X.) and the Helmsley Charitable Trust (to R.J.X.).

DATA AVAILABILITY

scRNA-seq data generated during this study are available under GEO accession code: GSE182767. Source data for the figures are provided in the individual source files. The reference mm10 mouse transcriptome was obtained from GENCODE: GCF_000001635.26.

REFERENCES

1. Wu H et al. T-cells produce acidic niches in lymph nodes to suppress their own effector functions. Nature communications 11, 4113 (2020).
2. Ihara Y et al. The G protein-coupled receptor T-cell death-associated gene 8 (TDAG8) facilitates tumor development by serving as an extracellular pH sensor. Proc Natl Acad Sci U S A 107, 17309–17314 (2010). [PubMed: 20855608]
3. Levin LR & Buck J Physiological roles of acid-base sensors. Annu Rev Physiol 77, 347–362 (2015). [PubMed: 25340964]
4. Ananthakrishnan AN et al. Environmental triggers in IBD: a review of progress and evidence. Nat Rev Gastroenterol Hepatol 15, 39–49 (2018). [PubMed: 29018271]
5. de Souza HS & Fiocchi C Immunopathogenesis of IBD: current state of the art. Nat Rev Gastroenterol Hepatol 13, 13–27 (2016). [PubMed: 26627550]
6. Kamada N, Seo SU, Chen GY & Nunez G Role of the gut microbiota in immunity and inflammatory disease. Nature reviews. Immunology 13, 321–335 (2013).
7. Hardin M et al. The clinical and genetic features of COPD-asthma overlap syndrome. Eur Respir J 44, 341–350 (2014). [PubMed: 24876173]
8. Wirasinha RC et al. GPR65 inhibits experimental autoimmune encephalomyelitis through CD4(+) T cell independent mechanisms that include effects on iNKT cells. Immunol Cell Biol 96, 128–136 (2018). [PubMed: 29363187]
9. International Multiple Sclerosis Genetics, C. et al. Genetic risk and a primary role for cell-mediated immune mechanisms in multiple sclerosis. Nature 476, 214–219 (2011). [PubMed: 21833088]
10. Lassen KG et al. Genetic Coding Variant in GPR65 Alters Lysosomal pH and Links Lysosomal Dysfunction with Colitis Risk. Immunity 44, 1392–1405 (2016). [PubMed: 27287411]
11. Franke A et al. Genome-wide meta-analysis increases to 71 the number of confirmed Crohn's disease susceptibility loci. Nat Genet 42, 1118–1125 (2010). [PubMed: 21102463]
12. Tcymbarevich I et al. Lack of the pH-sensing Receptor TDAG8 [GPR65] in Macrophages Plays a Detrimental Role in Murine Models of Inflammatory Bowel Disease. J Crohns Colitis 13, 245–258 (2019). [PubMed: 30535144]
13. Xie L et al. pH and Proton Sensor GPR65 Determine Susceptibility to Atopic Dermatitis. J Immunol 207, 101–109 (2021). [PubMed: 34135065]
14. Wang Y et al. The Proton-activated Receptor GPR4 Modulates Intestinal Inflammation. J Crohns Colitis 12, 355–368 (2018). [PubMed: 29136128]
15. de Valliere C et al. G Protein-coupled pH-sensing Receptor OGR1 Is a Regulator of Intestinal Inflammation. Inflamm Bowel Dis 21, 1269–1281 (2015). [PubMed: 25856770]
16. Basu R et al. Th22 cells are an important source of IL-22 for host protection against enteropathogenic bacteria. Immunity 37, 1061–1075 (2012). [PubMed: 23200827]
17. Ishigame H et al. Differential roles of interleukin-17A and −17F in host defense against mucoepithelial bacterial infection and allergic responses. Immunity 30, 108–119 (2009). [PubMed: 19144317]

18. Harbour SN, Maynard CL, Zindl CL, Schoeb TR & Weaver CT Th17 cells give rise to Th1 cells that are required for the pathogenesis of colitis. Proc Natl Acad Sci U S A 112, 7061–7066 (2015). [PubMed: 26038559]
19. Ivanov II et al. The orphan nuclear receptor RORgammat directs the differentiation program of proinflammatory IL-17+ T helper cells. Cell 126, 1121–1133 (2006). [PubMed: 16990136]
20. Plank MW et al. Th22 Cells Form a Distinct Th Lineage from Th17 Cells In Vitro with Unique Transcriptional Properties and Tbet-Dependent Th1 Plasticity. Journal of immunology 198, 2182–2190 (2017).
21. Wang C et al. CD5L/AIM Regulates Lipid Biosynthesis and Restrains Th17 Cell Pathogenicity. Cell 163, 1413–1427 (2015). [PubMed: 26607793]
22. Santori FR et al. Identification of natural RORgamma ligands that regulate the development of lymphoid cells. Cell Metab 21, 286–298 (2015). [PubMed: 25651181]
23. Orth JD, Thiele I & Palsson BO What is flux balance analysis? Nat Biotechnol 28, 245–248 (2010). [PubMed: 20212490]
24. Chitraju C et al. Triglyceride Synthesis by DGAT1 Protects Adipocytes from Lipid-Induced ER Stress during Lipolysis. Cell Metab 26, 407–418 e403 (2017). [PubMed: 28768178]
25. Dozsa A et al. PPARgamma-mediated and arachidonic acid-dependent signaling is involved in differentiation and lipid production of human sebocytes. J Invest Dermatol 134, 910–920 (2014). [PubMed: 24129064]
26. Rudloff I, Bachmann M, Pfeilschifter J & Muhl H Mechanisms of rapid induction of interleukin-22 in activated T cells and its modulation by cyclosporin a. J Biol Chem 287, 4531–4543 (2012). [PubMed: 22170067]
27. Bruno NE et al. Creb coactivators direct anabolic responses and enhance performance of skeletal muscle. The EMBO journal 33, 1027–1043 (2014). [PubMed: 24674967]
28. Riccio A, Ahn S, Davenport CM, Blendy JA & Ginty DD Mediation by a CREB family transcription factor of NGF-dependent survival of sympathetic neurons. Science 286, 2358–2361 (1999). [PubMed: 10600750]
29. Berod L et al. De novo fatty acid synthesis controls the fate between regulatory T and T helper 17 cells. Nat Med 20, 1327–1333 (2014). [PubMed: 25282359]
30. Chitraju C, Walther TC & Farese RV Jr. The triglyceride synthesis enzymes DGAT1 and DGAT2 have distinct and overlapping functions in adipocytes. J Lipid Res 60, 1112–1120 (2019). [PubMed: 30936184]
31. Nguyen TB et al. DGAT1-Dependent Lipid Droplet Biogenesis Protects Mitochondrial Function during Starvation-Induced Autophagy. Dev Cell 42, 9–21 e25 (2017). [PubMed: 28697336]
32. O'Connor W Jr. et al. A protective function for interleukin 17A in T cell-mediated intestinal inflammation. Nat Immunol 10, 603–609 (2009). [PubMed: 19448631]
33. Mogi C et al. Involvement of proton-sensing TDAG8 in extracellular acidification-induced inhibition of proinflammatory cytokine production in peritoneal macrophages. J Immunol 182, 3243–3251 (2009). [PubMed: 19234222]
34. Hipolito VEB et al. Enhanced translation expands the endo-lysosome size and promotes antigen presentation during phagocyte activation. PLoS Biol 17, e3000535 (2019). [PubMed: 31800587]
35. Mindell JA Lysosomal acidification mechanisms. Annu Rev Physiol 74, 69–86 (2012). [PubMed: 22335796]
36. Yambire KF et al. Impaired lysosomal acidification triggers iron deficiency and inflammation in vivo. Elife 8 (2019).
37. Alloatti A et al. Toll-like Receptor 4 Engagement on Dendritic Cells Restrains Phago-Lysosome Fusion and Promotes Cross-Presentation of Antigens. Immunity 43, 1087–1100 (2015). [PubMed: 26682983]
38. Xia Y et al. The Mevalonate Pathway Is a Druggable Target for Vaccine Adjuvant Discovery. Cell 175, 1059–1073 e1021 (2018). [PubMed: 30270039]
39. Graham DB et al. ITAM signaling in dendritic cells controls T helper cell priming by regulating MHC class II recycling. Blood 116, 3208–3218 (2010). [PubMed: 20634378]

40. Buckley CD, Gilroy DW, Serhan CN, Stockinger B & Tak PP The resolution of inflammation. Nature reviews. Immunology 13, 59–66 (2013).
41. Gagliani N et al. Th17 cells transdifferentiate into regulatory T cells during resolution of inflammation. Nature 523, 221–225 (2015). [PubMed: 25924064]
42. Schett G & Neurath MF Resolution of chronic inflammatory disease: universal and tissue-specific concepts. Nature communications 9, 3261 (2018).
43. Cartwright IM et al. Adaptation to inflammatory acidity through neutrophil-derived adenosine regulation of SLC26A3. Mucosal Immunol 13, 230–244 (2020). [PubMed: 31792360]
44. Hua S Advances in Oral Drug Delivery for Regional Targeting in the Gastrointestinal Tract - Influence of Physiological, Pathophysiological and Pharmaceutical Factors. Front Pharmacol 11, 524 (2020). [PubMed: 32425781]
45. Nugent SG, Kumar D, Rampton DS & Evans DF Intestinal luminal pH in inflammatory bowel disease: possible determinants and implications for therapy with aminosalicylates and other drugs. Gut 48, 571–577 (2001). [PubMed: 11247905]
46. Gaublomme JT et al. Single-Cell Genomics Unveils Critical Regulators of Th17 Cell Pathogenicity. Cell 163, 1400–1412 (2015). [PubMed: 26607794]
47. Miyazaki M, Dobrzyn A, Elias PM & Ntambi JM Stearoyl-CoA desaturase-2 gene expression is required for lipid synthesis during early skin and liver development. Proc Natl Acad Sci U S A 102, 12501–12506 (2005). [PubMed: 16118274]
48. van Dierendonck X et al. HILPDA Uncouples Lipid Droplet Accumulation in Adipose Tissue Macrophages from Inflammation and Metabolic Dysregulation. Cell Rep 30, 1811–1822 e1816 (2020). [PubMed: 32049012]
49. Geltink RIK, Kyle RL & Pearce EL Unraveling the Complex Interplay Between T Cell Metabolism and Function. Annu Rev Immunol 36, 461–488 (2018). [PubMed: 29677474]
50. Suzuki H, Kumagai T, Goto A & Sugiura T Increase in intracellular hydrogen peroxide and upregulation of a nuclear respiratory gene evoked by impairment of mitochondrial electron transfer in human cells. Biochem Biophys Res Commun 249, 542–545 (1998). [PubMed: 9712733]
51. Havlickova Karbanova V et al. Compensatory upregulation of respiratory chain complexes III and IV in isolated deficiency of ATP synthase due to TMEM70 mutation. Biochim Biophys Acta 1817, 1037–1043 (2012). [PubMed: 22433607]
52. Howie D et al. A Novel Role for Triglyceride Metabolism in Foxp3 Expression. Front Immunol 10, 1860 (2019). [PubMed: 31456800]
53. Gutierrez-Vazquez C & Quintana FJ Regulation of the Immune Response by the Aryl Hydrocarbon Receptor. Immunity 48, 19–33 (2018). [PubMed: 29343438]
54. Delamarre L, Pack M, Chang H, Mellman I & Trombetta ES Differential lysosomal proteolysis in antigen-presenting cells determines antigen fate. Science 307, 1630–1634 (2005). [PubMed: 15761154]
55. Trost M et al. The phagosomal proteome in interferon-gamma-activated macrophages. Immunity 30, 143–154 (2009). [PubMed: 19144319]

METHODS-ONLY REFERENCES

56. Graham DB et al. Antigen discovery and specification of immunodominance hierarchies for MHCII-restricted epitopes. Nat Med 24, 1762–1772 (2018). [PubMed: 30349087]
57. Fleming SJ, Marioni JC & Babadi M CellBender remove-background: a deep generative model for unsupervised removal of background noise from scRNA-seq datasets. bioRxiv 791699 (2019).
58. Korsunsky I et al. Fast, sensitive and accurate integration of single-cell data with Harmony. Nat Methods 16, 1289–1296 (2019). [PubMed: 31740819]
59. Wagner A et al. Metabolic modeling of single Th17 cells reveals regulators of autoimmunity. Cell 184, 4168–4185 e4121 (2021). [PubMed: 34216539]
60. Seki A & Rutz S Optimized RNP transfection for highly efficient CRISPR/Cas9-mediated gene knockout in primary T cells. J Exp Med 215, 985–997 (2018). [PubMed: 29436394]

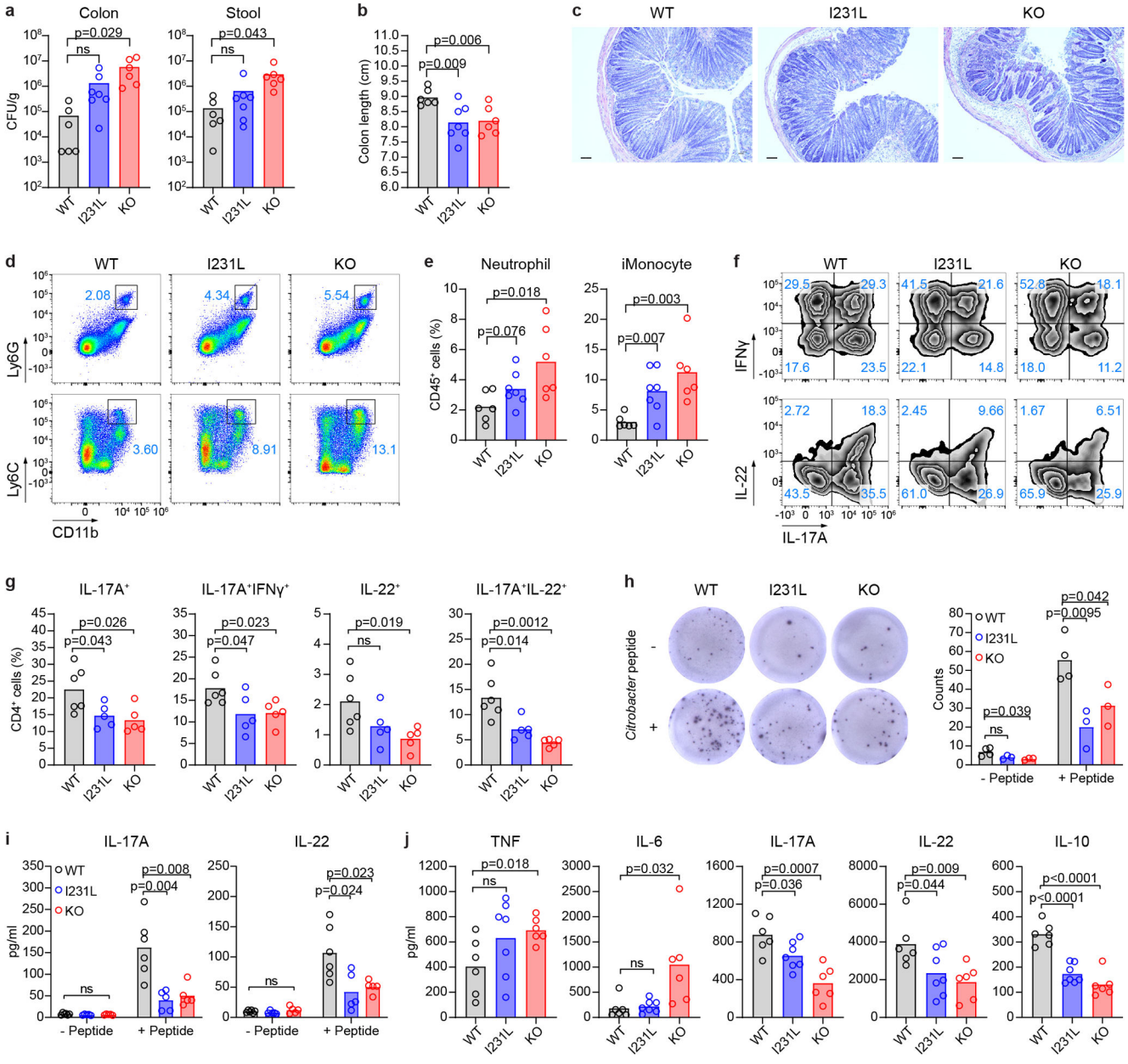

Figure 1. GPR65 I231L exacerbates bacterial infection-induced colitis.

(a,b) Colony-forming units (CFU) in the colon and stool (a) and colon length (b) on day 12 after *C. rodentium* infection. **(c)** H&E-stained sections of distal colon from infected mice. Representative images from one of two independent experiments. **(d,e)** Immunophenotyping of neutrophils ($CD11b^+Ly6G^+$) and inflammatory monocytes ($CD11b^+Ly6C^+$) in the colonic lamina propria (LP). **(f, g)** Cytokine profiles of $CD4^+$ T cells from the colonic LP on day 12 after infection. **(h)** IL-17A ELISPOT profiles of cells isolated from the mesenteric lymph node (mLN) on day 7 after infection. **(i)** IL-17A and IL-22 production from mLN cells with or without *Citrobacter* peptide stimulation as in (h). **(j)** Cytokine profiles of colonic tissue from infected mice. Scale bar, 0.5mm. Data are mean values (a,b,e,g-j). $n_{WT}=6$; $n_{I231L}=7$;

n_{KO}=6 mice (a,b,e,j). n_{WT}=6; n_{I231L}=5; n_{KO}=5 mice (g,i). n_{WT}=4; n_{I231L}=3; n_{KO}=3 mice (h). P values determined by unpaired two-tailed t-test; ns, not significant. Data represent at least two independent experiments.

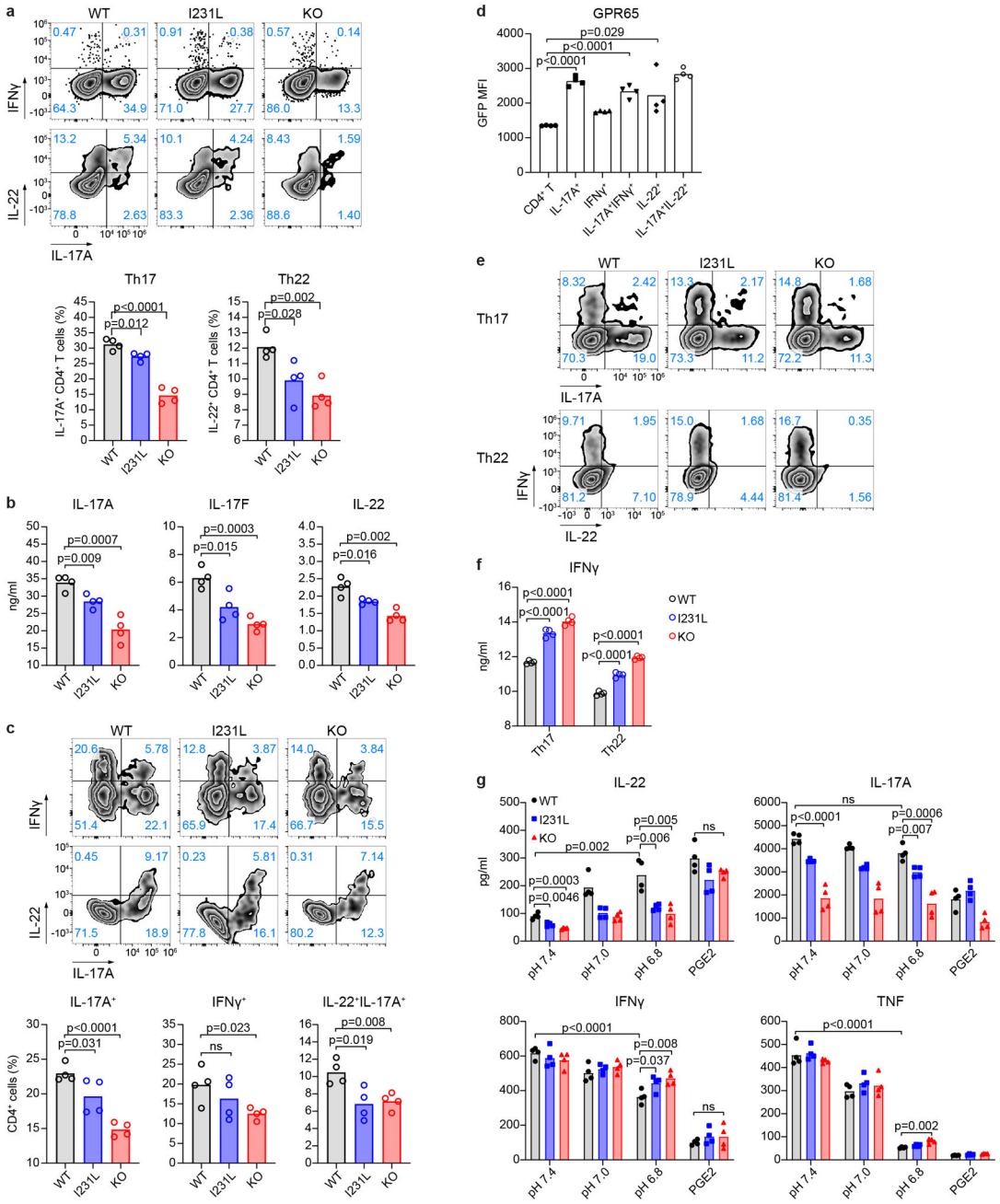

Figure 2. GPR65 I231L affects Th17 and Th22 polarization and pH-dependent release of IL-22.

(a,b) *In vitro* polarization of Th17 and Th22 cells from CD4$^+$ T cells. Cytokines from culture supernatants were detected. **(c)** Cytokine profiles of IL-17A- and/or IL-22-producing Th cells from the small intestinal LP at homeostasis. **(d)** GPR65 expression levels by GFP mean fluorescence intensity (MFI) in Th subsets as in (c). IRES-EGFP sequences replaced exon 2 coding sequence under *Gpr65* promoters in KO mice. **(e,f)** Th17 and Th22 cell repolarization under Th1 polarization conditions. **(g)** Cytokine responses to pH and prostaglandin E2 (PGE2, 0.5μM) in Th cells polarized *in vitro*. IL-22, IL-17A, IFNγ, TNF

measured from culture supernatants of Th22, Th17, Th1 and Th0 cells, respectively, after restimulation. Data are mean values (a-d,f,g). n=4 biological replicates per group (a-d,f,g). P values determined by unpaired two-tailed t-test; ns, not significant. Data represent at least two independent experiments.

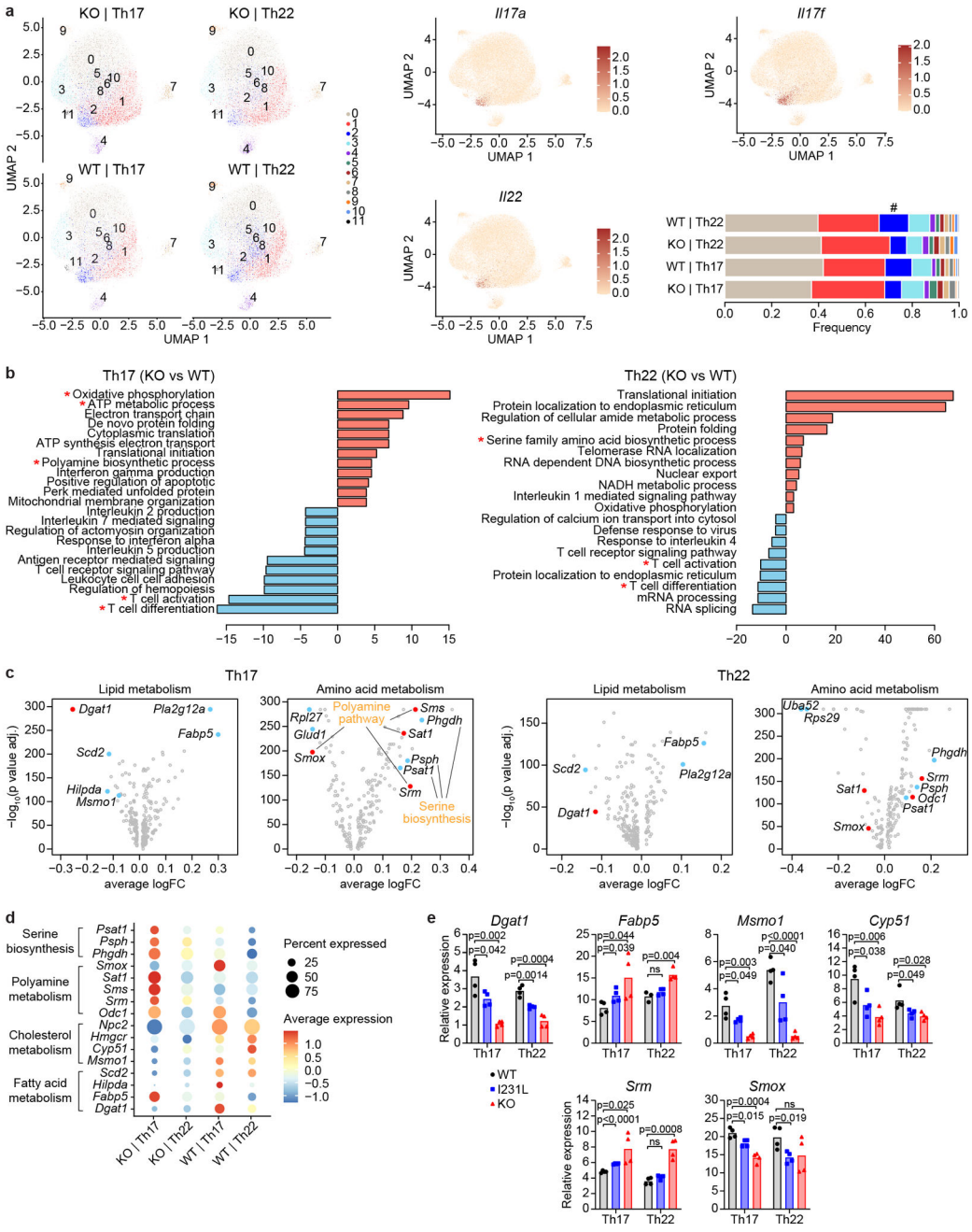

Figure 3. Single-cell RNA-sequencing reveals cellular metabolism changes in *Gpr65*-null Th17 and Th22 cells.

(a) Uniform manifold approximation and projection (UMAP) embeddings of single-cell RNA-sequencing profiles from *in vitro* polarized Th17 (n_{WT}=22,281; n_{KO}=29,102) and Th22 (n_{WT}=27,423; n_{KO}=25,854) cells. Expression of *Il17a*, *Il17f* and *Il22* and proportion of different clusters are shown. Hash marks cluster 2. **(b)** Enrichment of gene ontology biological processes signature scores in cluster 2 transcriptomes. **(c)** Differential expression (KO versus WT) of genes related

to lipid metabolism (REACTOME_METABOLISM_OF_LIPIDS) and amino acid metabolism (REACTOME_METABOLISM_OF_AMINO_ACIDS_AND_DERIVATIVES). **(d)** Differential expression of genes related to metabolic processes in cluster 2 transcriptomes. **(e)** qPCR validation of differential gene expression. Data are mean values representing two independent experiments. n=4 biological replicates for each group. P values determined by unpaired two-tailed t-test; ns, not significant.

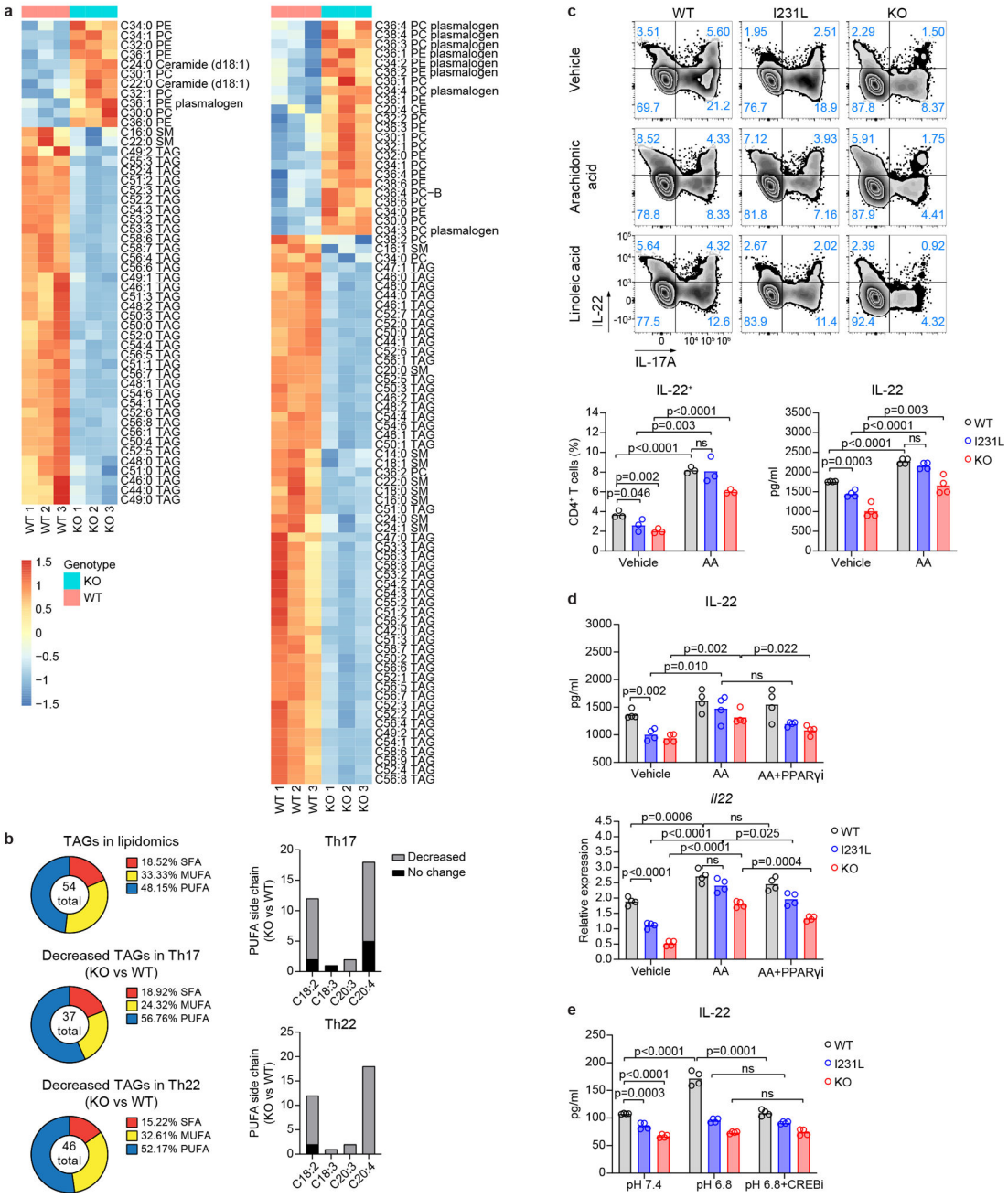

Figure 4. Fatty acid composition and triacylglyceride storage changes in *Gpr65*-null Th17 and Th22 cells.

(a) Differential metabolites from lipidomic analysis of *in vitro* polarized Th17 and Th22 cells. See Extended Data Fig. 6 for all lipid metabolites. **(b)** Left, Fatty acid side chain distribution in all detected TAGs and TAGs decreased in KO cells. Right, PUFA lipids in TAGs decreased in KO cells. **(c,d)** *In vitro* polarization of Th22 cells treated with PUFAs (10μM arachidonic or linoleic acid, c) or PPARγ inhibitor (2μM PPARγi, d) on day 1. Intracellular cytokine analysis, IL-22 detection in culture supernatant and qPCR performed

on day 3. **(e)** IL-22 production 24h after treatment with CREB inhibitor (CREBi, 100nM) at low pH. Data are mean values representing at least two independent experiments (c-e). n=3 ($IL\text{-}22^+$ in c) or n=4 biological replicates per group (c-e). P values determined by unpaired two-tailed t-test; ns, not significant.

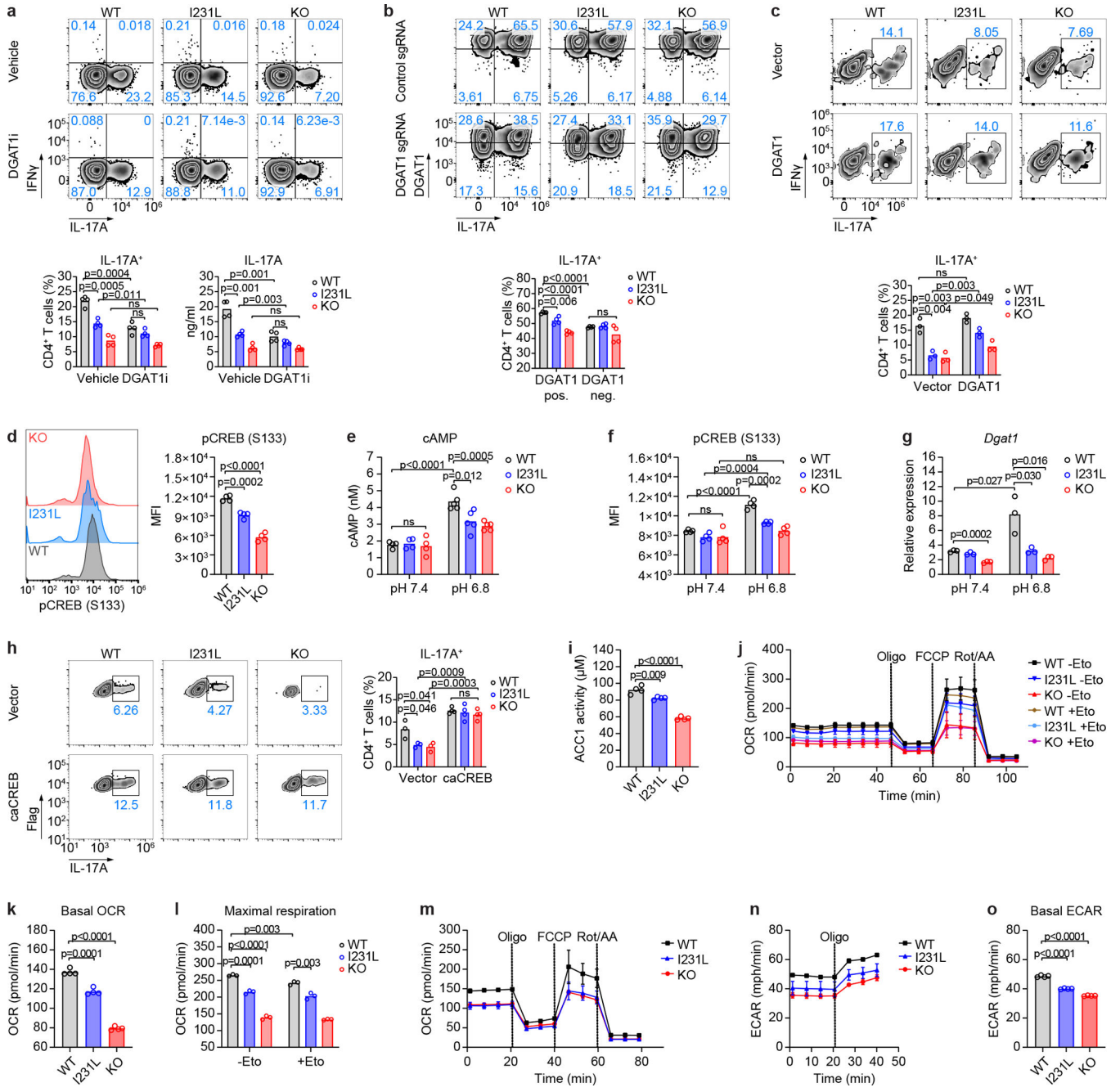

Figure 5. GPR65 I231L modulates Th17 differentiation through the cAMP-CREB-DGAT1 axis.

(a,b) Th17 polarization with DGAT1 inhibitor (DGAT1i, 1μM) (a) or DGAT1 KO (b). Intracellular cytokine or DGAT1 staining profiles (day 3) and culture supernatant IL-17A shown. n=4 biological replicates per group. **(c)** Th17 polarization with DGAT1 overexpression. Naïve $CD4^+$ T cells transfected (day 1) and stained for intracellular cytokines (day 3). Cells pre-gated by DGAT1 expression ($mRFP1^+$). n=3 biological replicates per group. **(d)** Phosphoflow of phospho-CREB (S133) on day 3 of Th17 polarization. n=4 biological replicates per group. **(e,f)** cAMP level (e) and CREB phosphorylation (f) in Th0 cells under neutral or acidic pH (30min). n=4 (pH 7.4) or n=5

(pH 6.8) biological replicates per group (e); n=4 biological replicates per group (f). **(g)** *Dgat1* expression by qPCR in Th17 cells under neutral or acidic pH (2h). n=3 biological replicates per group. **(h)** Th17 polarization with constitutively active CREB (caCREB). Cells prepared as in (c) and pre-gated by caCREB expression ($Flag^+$). n=3 (vector) or n=4 (caCREB) biological replicates per group. **(i)** ACC1 activity in day 3 polarized Th17 cells. n=4 biological replicates per group. **(j-m)** $CD4^+$ T cells stimulated under Th17 polarization condition (24h), then treated in substrate-limited growth media (18h). Cells pretreated with etomoxir (Eto, 4μM) before palmitate oxidation detection (j). OCRs monitored after oligomycin (Oligo, 1.5μM), carbonyl cyanide-4-(trifluoromethoxy) phenylhydrazone (FCCP, 1.5μM), and rotenone and antimycin A (Rot/AA, 0.5μM) addition. Basal (k) and maximal respiration (l) OCR quantified. Mitochondrial respiration detected in day 2 polarized Th17 cells without pretreatments (m). n=4 (j,k,m) and n=3 (l) biological replicates per group. **(n,o)** ECAR monitored as in (m), and basal ECAR quantified. n=4 biological replicates per group. Data are mean values (a-o) ±SD (j,m,n). P values determined by unpaired two-tailed t-test; ns, not significant. Data represent at least two independent experiments.

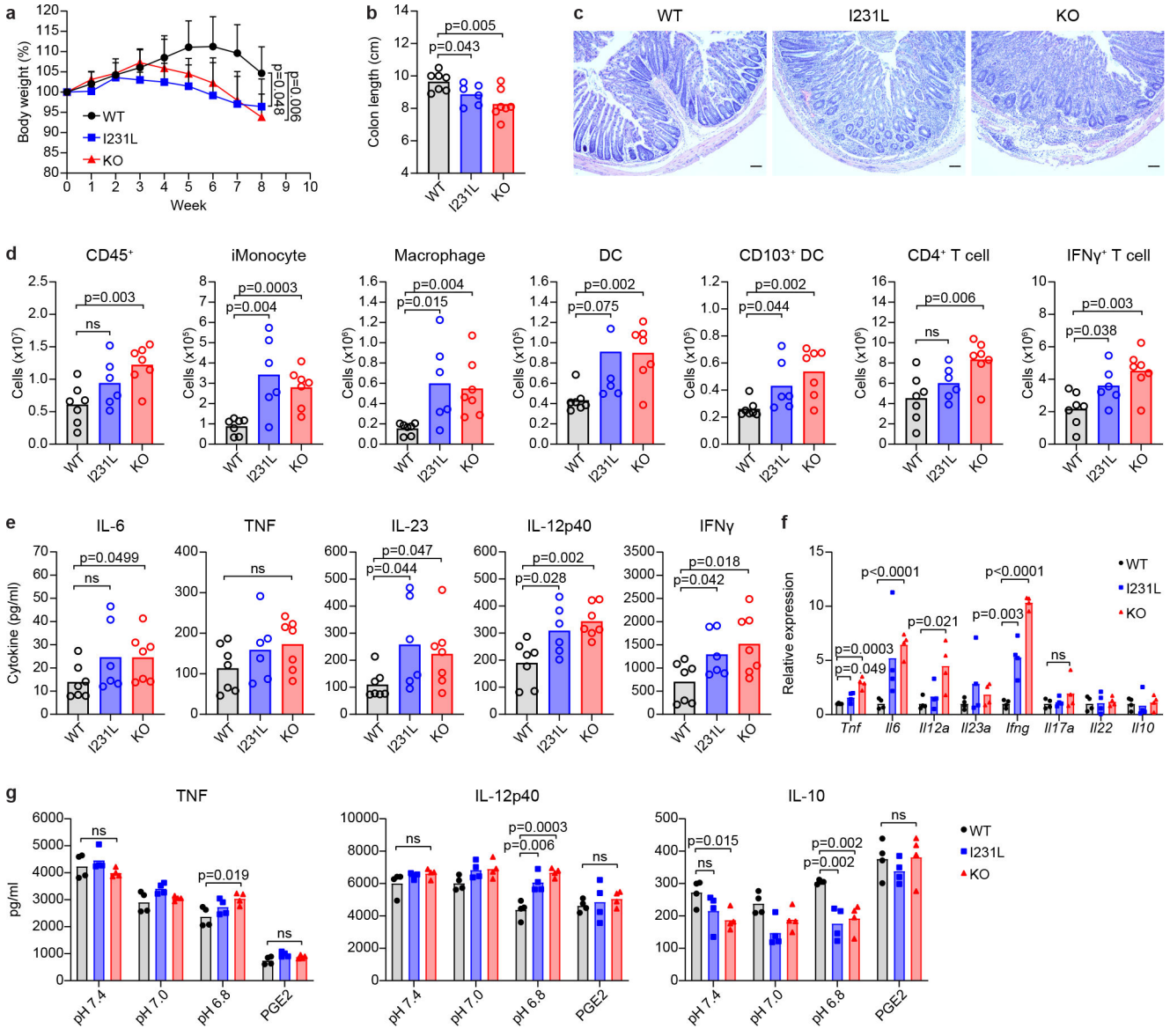

Figure 6. GPR65 I231L promotes T cell-driven colitis with elevated inflammatory cytokine release.

(a,b) Body weight changes (a) and colon length (b) of WT, I231L and KO mice (*Rag1* KO background) after transfer of WT CD4$^+$ T cells. **(c)** H&E-stained sections of distal colon from mice with T cell-driven colitis. Representative images from one of two independent experiments. Scale bar, 0.5mm. **(d)** Quantification of myeloid and CD4$^+$ T cells in the colonic LP of mice in (a) 8 weeks after colitis induction. **(e,f)** Cytokine profiles of colonic tissue detected by multiplex bead-based cytokine assay (e) and qPCR (f). **(g)** Cytokine responses of WT, I231L and KO BMDCs under different pH and PGE2 (0.5μM) stimulation upon activation by LPS (20ng/ml). Data are mean values (a,b,d-g) + SEM (a). n_{WT}=7; n_{I231L}=6; n_{KO}=8 mice (a). n_{WT}=7; n_{I231L}=6; n_{KO}=7 mice (b,d,e). n_{WT}=4; n_{I231L}=4; n_{KO}=4 mice (f,g). P values determined by unpaired two-tailed t-test; ns, not significant. Data represent at least two independent experiments.

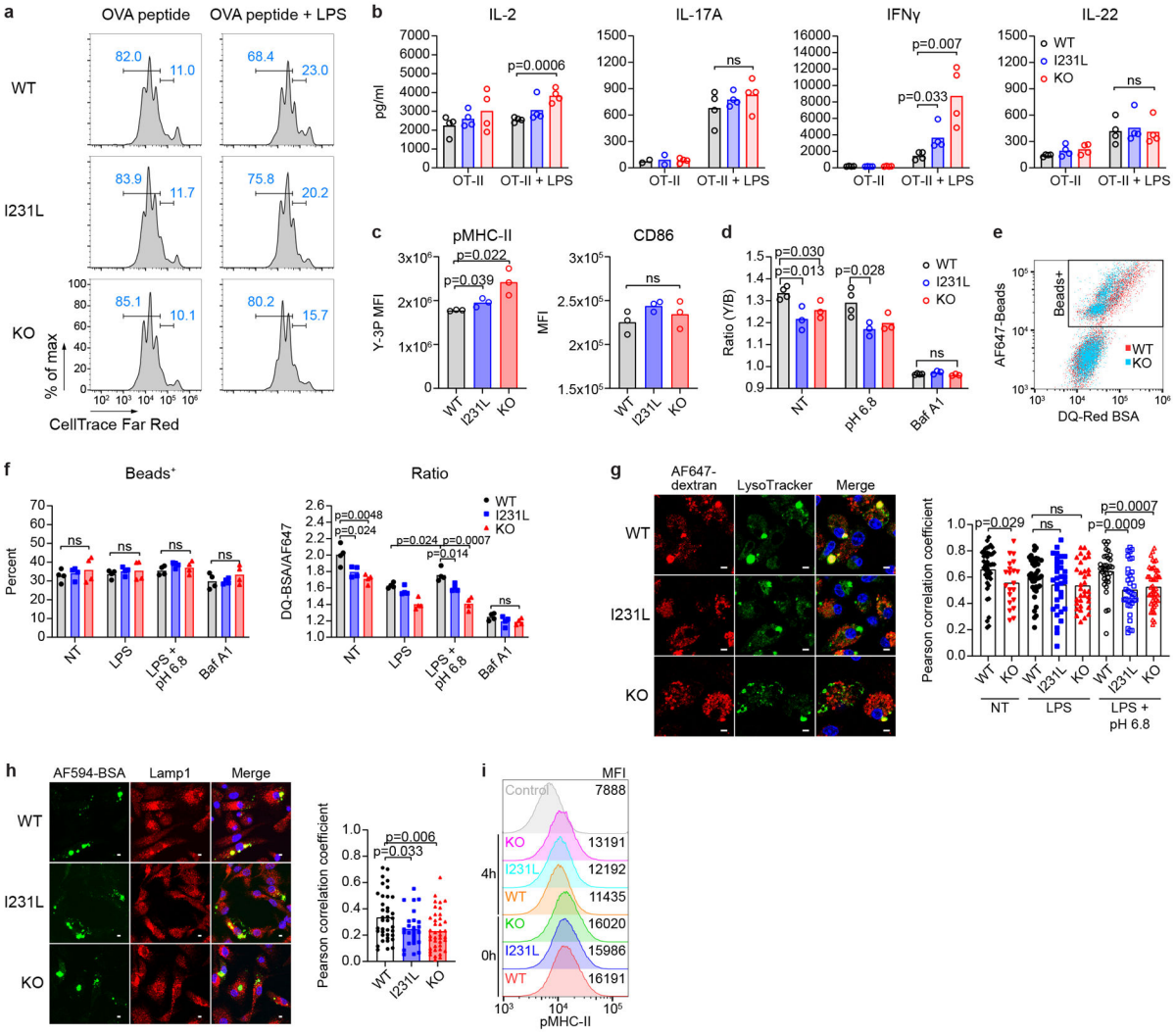

Figure 7. GPR65 I231L enhances antigen presentation in dendritic cells by influencing endo-lysosomal fusion and degradation capacity.

(a) Representative profiles of divided OT-II T cells in a BMDC:OT-II T cell co-culturing-based antigen presentation assay (day 3). **(b,c)** Cytokines in culture supernatants (b), pMHC-II complex and CD86 expression in BMDCs (c) from assay in (a). n=4 (b) and n=3 (c) biological replicates per group. **(d)** Ratio of dual emissions from pH indicator LysoSensor Yellow/Blue. Lower Y/B ratio indicates increased pH. NT, no treatment; Baf A1, bafilomycin A1 (20nM, 2h), a specific V-ATPase inhibitor that blocks lysosomal acidification, serves as a control. n=4 (WT) and n=3 (I231L, KO) biological replicates per condition. **(e,f)** Endocytosis and protein degradation in BMDCs treated with DQ-Red BSA and Alexa Fluor 647 dye conjugated fluorescent beads monitored by flow cytometry. Representative flow profiles of BMDCs incubated with beads without other treatment (e). Statistical analysis of endocytosis in BMDCs indicated by beads^{+} percentage and proteolytic capacity indicated by ratio of DQ-Red BSA and AF647 fluorescence intensities; n=4 biological replicates per group (f). **(g,h)** Endo-lysosome fusion in BMDCs detected by

microscopy. Representative images of BMDCs treated with LPS at low pH from one of three independent experiments. At least 6 fields were analyzed for each group. n_{WT}=43, n_{KO}=21 (NT); n_{WT}=40, n_{I231L}=33, n_{KO}=34 (LPS); n_{WT}=34, n_{I231L}=36, n_{KO}=46 (LPS+pH6.8) cells (g). n_{WT}=38, n_{I231L}=26, n_{KO}=40 cells (h). Statistical analysis of endosome and lysosome colocalization indicated by Pearson correlation coefficient. Scale bar, 4.2μm. Blue, DAPI. **(i)** Half-life of pMHC-II complex monitored by flow cytometry. pMHC-II complex was enriched by immunoprecipitation from BMDCs after surface biotinylation with or without chase for 4h, then detected with AF647- streptavidin. Data are mean values (b-d,f-h). P values determined by unpaired two-tailed t-test; ns, not significant. Representative data from at least two independent experiments.